

# Solving integral equations on piecewise smooth boundaries using the RCIP method: a tutorial

Johan Helsing

*Centre for Mathematical Sciences*

*Lund University, Box 118, SE-221 00 Lund, Sweden*

(revised and enlarged October 6, 2017)

## Abstract

Recursively Compressed Inverse Preconditioning (RCIP) is a numerical method for solving Fredholm second kind boundary integral equations in situations where the boundary shape induces a non-smooth behavior in the solution. The method originated in 2008 within a scheme for Laplace's equation in two-dimensional domains with corners. In a series of subsequent papers the method was then refined and extended as to apply to integral equation formulations of a broad range of boundary value problems in physics and engineering. The purpose of the present tutorial is threefold: First, to review the RCIP method in a simple setting. Second, to show how easily the method can be implemented in MATLAB. Third, to present new applications.

## 1 Introduction

This tutorial is about an efficient numerical solver for elliptic boundary value problems in domains whose boundaries contain some sort of singular points. Such a solver is useful for applications in physics and engineering, where computational domains of interest often have corners, triple junctions, and close-to-touching boundary parts. Furthermore, these problems are difficult to solve irrespective of what numerical method is used. The reason being that the solution, or the quantity representing the solution, often exhibits a non-smooth behavior close to boundary singularities. That behavior is hard to resolve by polynomials, which underlie most approximation schemes. Mesh refinement is needed. This is costly and may lead to artificial ill-conditioning and the loss of accuracy.

The numerical solver we propose takes its starting point in an integral equation reformulation of the boundary value problem at hand. We assume that the problem can be modeled as a Fredholm second kind integral equation with integral operators that are compact away from singular boundary

points and whose solution is a layer density representing the solution to the original problem. We then seek a discrete approximation to the layer density using a modification of Nyström discretization [2, Chapter 4]. At the heart of the solver lie certain integral transforms whose inverses modify the kernels of the integral operators in such a way that the layer density becomes piecewise smooth and simple to resolve by polynomials. The discretizations of the inverses are constructed recursively on locally refined temporary meshes. Conceptually, this corresponds to applying a fast direct solver [40] locally to regions with troublesome geometry. Finally, a global iterative method is applied. This gives us many of the advantages of fast direct methods, for example the ability to deal with certain classes of operators whose spectra make them unsuitable for iterative methods. In addition, the approach is typically much faster than using only a fast direct solver.

Our method, or scheme, has been referred to as *recursive compressed inverse preconditioning* [21, 22, 31, 32] and there is a good reason for that name: the scheme relies on applying a relieving right inverse to the integral equation; on compressing this inverse to a low-dimensional subspace; and on carrying out the compression in a recursive manner. Still, the name *recursive(ly) compressed inverse preconditioning* is a bit awkward and we will here simply use the acronym RCIP.

A strong motivation for writing the present tutorial is that the original references [21, 22, 31, 32] are hard to read and that efficient codes, therefore, could be hard to implement. Certain derivations in [21, 22, 31, 32] use complicated intermediary constructions, application specific issues obscure the general picture, and the notation has evolved from paper to paper. Here we focus on the method itself, on how it works and how it can be implemented, and refer to the original research papers for details. Demo programs in MATLAB, updated as of August 2017, are a part of the exposition and can be downloaded from the web page:

<http://www.maths.lth.se/na/staff/helsing/Tutor/>

Section 2 provides some historical background. The basics of the RCIP method are then explained by solving a simple model problem in Sections 3–6. Sections 7–16 review general algorithmic improvements. Sections 17–20 contain applications to scattering problems and Sections 21–25 deal with close-to-touching objects, mixed (Zaremba) boundary conditions, Steklov eigenvalue problems, limit polarizability, and vertex singularity exponents. Some of this material is new and has not been published elsewhere.

## 2 Background

The line of research on fast solvers for elliptic boundary value problems in piecewise smooth domains, leading up to the RCIP method, grew out of work in computational fracture mechanics. Early efforts concerned find-

ing efficient integral equation formulations. Corner singularities were either resolved with brute force or by using special basis functions [20, 26, 35]. Such strategies, in combination with fast multipole [15] accelerated iterative solvers, work well for simple small-scale problems.

Real world physics is more complicated and, for example, the study [12] on a high-order time-stepping scheme for crack propagation (a series of biharmonic problems for an evolving piecewise smooth surface) shows that radically better methods are needed. Special basis functions are too complicated to construct and brute force is not economical – merely storing the discretized solution becomes too costly in a large-scale simulation.

A breakthrough came in 2007, when a scheme was created that resolves virtually any problem for Laplace’s equation in piecewise smooth two-dimensional domains in a way that is fully automatic, fast, stable, memory efficient, and whose computational cost scales linearly with the number of corners in the computational domain. The resulting paper [31] constitutes the origin of the RCIP method. Unfortunately, however, there are some flaws in [31]. For example, the expressions in [31, Section 9] are not generally valid and the paper fails to apply RCIP in its entirety to the biharmonic problem of [31, Section 3], which was the ultimate goal.

The second paper on RCIP [32] deals with elastic grains. The part [32, Appendix B], on speedup, is particularly useful.

The third paper on RCIP [21] contains improvement relative to the earlier papers, both in the notation and in the discretization of singular operators. The overall theme is mixed boundary conditions, which pose similar difficulties as do piecewise smooth boundaries.

The paper [22], finally, solves the problem of [31, Section 3] in a broad setting and one can view the formalism of [22] as the RCIP method in its most general form, at least in two dimensions. Further work on RCIP has been devoted to more general boundary conditions [45], to problems in three dimension [28, 33, 34], and to solving elliptic boundary value problems in special situations, such as for aggregates of millions of grains, where special techniques are introduced to deal with problem specific issues [23, 24].

We end this retrospection by noting that several research groups in recent years have proposed numerical schemes for integral equations stemming from elliptic partial differential equations (PDEs) in domains with boundary singularities. See, for example, [1, 3, 4, 5, 6, 7, 8, 47]. There is also a widespread notion that a slight rounding of corners is a good idea for numerics. While rounding may work in particular situations, we do not believe it is a generally viable method. For one thing, how does one round a triple junction?

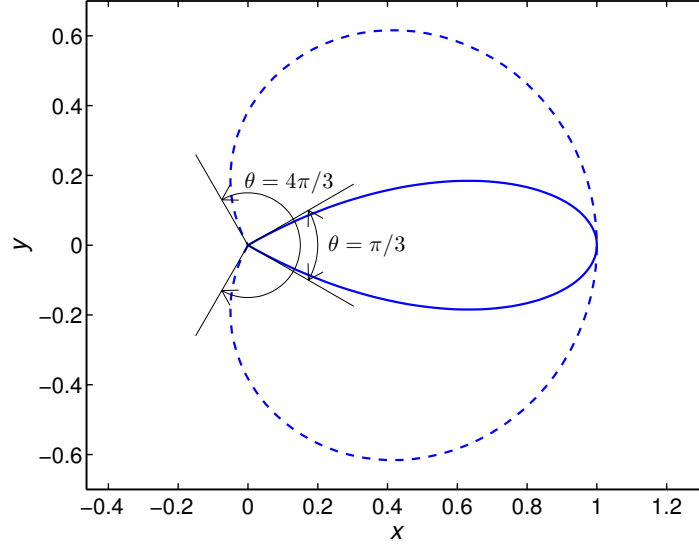


Figure 1: The contour  $\Gamma$  of (1) with a corner at the origin. The solid curve corresponds to opening angle  $\theta = \pi/3$ . The dashed curve has  $\theta = 4\pi/3$ .

### 3 A one-corner model problem

Let  $\Gamma$  be the closed contour of Figure 1 with the parameterization

$$r(s) = \sin(\pi s) (\cos((s - 0.5)\theta), \sin((s - 0.5)\theta)) , \quad s \in [0, 1] . \quad (1)$$

Let  $G(r, r')$  be the fundamental solution to Laplace's equation in the plane:

$$G(r, r') = -\frac{1}{2\pi} \log |r - r'| . \quad (2)$$

We shall solve the integral equation

$$\rho(r) + 2\lambda \int_{\Gamma} \frac{\partial G}{\partial \nu}(r, r') \rho(r') d\ell' = 2\lambda (e \cdot \nu) , \quad r \in \Gamma , \quad (3)$$

numerically for the unknown layer density  $\rho(r)$ . Here  $\nu$  is the exterior unit normal at  $r \in \Gamma$ ,  $d\ell$  is an element of arc length,  $\lambda$  is a parameter,  $e$  is a unit vector, and

$$\frac{\partial G}{\partial \nu}(r, r') = \frac{\nu \cdot (r' - r)}{2\pi |r' - r|^2} . \quad (4)$$

The equation (3) models an electrostatic transmission problem [31] where  $e$  is an applied electric field.

Using complex notation, where vectors  $r$ ,  $r'$ ,  $\nu$ , and  $e$  in the real plane  $\mathbb{R}^2$  correspond to points  $z$ ,  $\tau$ ,  $n$ , and  $e$  in the complex plane  $\mathbb{C}$ , one can write (3) as

$$\rho(z) + \frac{\lambda}{\pi} \int_{\Gamma} \rho(\tau) \Im \left\{ \frac{n_z \bar{n}_\tau d\tau}{\tau - z} \right\} = 2\lambda \Re \{ \bar{e} n_z \} , \quad z \in \Gamma , \quad (5)$$

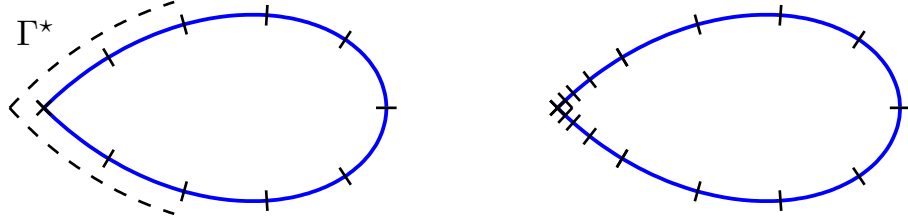


Figure 2: Left: A coarse mesh with ten panels on the contour  $\Gamma$  of (1) with opening angle  $\theta = \pi/2$ . A subset of  $\Gamma$ , called  $\Gamma^*$ , covers four coarse panels as indicated by the dashed curve. Right: A fine mesh created from the coarse mesh by subdividing the panels closest to the corner  $n_{\text{sub}} = 3$  times.

where the overbar symbol denotes the complex conjugate. Equation (5) is a simplification over (3) from a programming point of view.

In many contexts it is advantageous to abbreviate (3) as

$$(I + \lambda K) \rho(r) = \lambda g(r), \quad r \in \Gamma, \quad (6)$$

where  $I$  is the identity. If  $\Gamma$  is smooth, then (6) is a Fredholm second kind integral equation with a compact, non-self-adjoint, integral operator  $K$  whose spectrum is discrete, bounded by one in modulus, and accumulates at zero.

We also need a way to monitor the convergence of solutions  $\rho(r)$  to (6). For this purpose we introduce a quantity  $q$ , which corresponds to dipole moment or (un-normalized) polarizability [33]

$$q \equiv \int_{\Gamma} \rho(r) (e \cdot r) d\ell = \int_{\Gamma} \rho(z) \Re \{ \bar{e} z \} d|z|. \quad (7)$$

**Remark:** Existence issues are important. Loosely speaking, the boundary value problem modeled by (3) has a unique finite-energy solution for a large class of non-smooth  $\Gamma$  when  $\lambda$  is either off the real axis or when  $\lambda$  is real and  $\lambda \in [-1, 1)$ . See [33] for sharper statements. The precise meaning of a *numerical solution* to an integral equation such as (3) also deserves comment. In this paper, a numerical solution refers to approximate values of  $\rho(r)$  at a discrete set of points  $r_i \in \Gamma$ . The values  $\rho(r_i)$  should, in a post-processor, enable the extraction of quantities of interest including values of  $\rho(r)$  at arbitrary points  $r \in \Gamma$ , functionals of  $\rho(r)$  such as  $q$  of (7), and the solution to the underlying boundary value problem at points in the domain where that problem was set.

## 4 Discretization on two meshes

We discretize (6) using standard Nyström discretization based on composite 16-point Gauss–Legendre quadrature on two different meshes: a *coarse mesh*

with  $n_{\text{pan}}$  quadrature panels and a *fine mesh* which is constructed from the coarse mesh by  $n_{\text{sub}}$  times subdividing the panels closest to the corner in a direction toward the corner. The discretization is in parameter. The four panels on the coarse mesh that are closest to the corner should be equi-sized in parameter. These panels form a subset of  $\Gamma$  called  $\Gamma^*$ . See Figure 2.

The linear systems resulting from the discretization on the coarse mesh and on the fine mesh can be written formally as

$$(\mathbf{I}_{\text{coa}} + \lambda \mathbf{K}_{\text{coa}}) \boldsymbol{\rho}_{\text{coa}} = \lambda \mathbf{g}_{\text{coa}}, \quad (8)$$

$$(\mathbf{I}_{\text{fin}} + \lambda \mathbf{K}_{\text{fin}}) \boldsymbol{\rho}_{\text{fin}} = \lambda \mathbf{g}_{\text{fin}}, \quad (9)$$

where  $\mathbf{I}$  and  $\mathbf{K}$  are square matrices and  $\boldsymbol{\rho}$  and  $\mathbf{g}$  are column vectors. The subscripts fin and coa indicate what type of mesh is used. Discretization points on a mesh are said to constitute a *grid*. The coarse grid has  $n_p = 16n_{\text{pan}}$  points. The fine grid has  $n_p = 16(n_{\text{pan}} + 2n_{\text{sub}})$  points.

The discretization of (6) is carried out by first rewriting (5) as

$$\rho(z(s)) + \frac{\lambda}{\pi} \int_0^1 \rho(\tau(t)) \Re \left\{ \frac{n_{z(s)} |\dot{\tau}(t)| dt}{\tau(t) - z(s)} \right\} = 2\lambda \Re \{ \bar{e} n_{z(s)} \}, \quad s \in [0, 1], \quad (10)$$

where  $\dot{\tau}(t) = d\tau(t)/dt$ . Then Nyström discretization with  $n_p$  points  $z_i$  and weights  $w_i$  on  $\Gamma$  gives

$$\rho_i + \frac{\lambda}{\pi} \sum_{j=1}^{n_p} \rho_j \Re \left\{ \frac{n_i |\dot{z}_j| w_j}{z_j - z_i} \right\} = 2\lambda \Re \{ \bar{e} n_i \}, \quad i = 1, 2, \dots, n_p. \quad (11)$$

The program `demo1.m` sets up the system (9), solves it using the GMRES iterative solver [46] incorporating a low-threshold stagnation avoiding technique [30, Section 8], and computes  $q$  of (7). The user has to specify the opening angle  $\theta$ , the parameter  $\lambda$ , the number  $n_{\text{pan}}$  of coarse panels on  $\Gamma$ , the unit vector  $e$  and the number of subdivisions  $n_{\text{sub}}$ . The opening angle should be in the interval  $\pi/3 \leq \theta \leq 5\pi/3$ . We choose  $\lambda = 0.999$ ,  $\theta = \pi/2$ ,  $n_{\text{pan}} = 10$ , and  $e = (1, 0)$ . The quantity  $q$  converges initially as  $n_{\text{sub}}$  is increased, but for  $n_{\text{sub}} > 44$  the results start to get worse. See Figure 3. This is related to the fact, pointed out by Bremer [4], that standard Nyström discretization captures the  $L^\infty$  behavior of the solution  $\rho$ , while our  $\rho$  is unbounded. See, further, Appendix E.

## 5 Compressed inverse preconditioning

Let us split the matrices  $\mathbf{K}_{\text{coa}}$  and  $\mathbf{K}_{\text{fin}}$  of (8) and (9) into two parts each

$$\mathbf{K}_{\text{coa}} = \mathbf{K}_{\text{coa}}^* + \mathbf{K}_{\text{coa}}^\circ, \quad (12)$$

$$\mathbf{K}_{\text{fin}} = \mathbf{K}_{\text{fin}}^* + \mathbf{K}_{\text{fin}}^\circ. \quad (13)$$

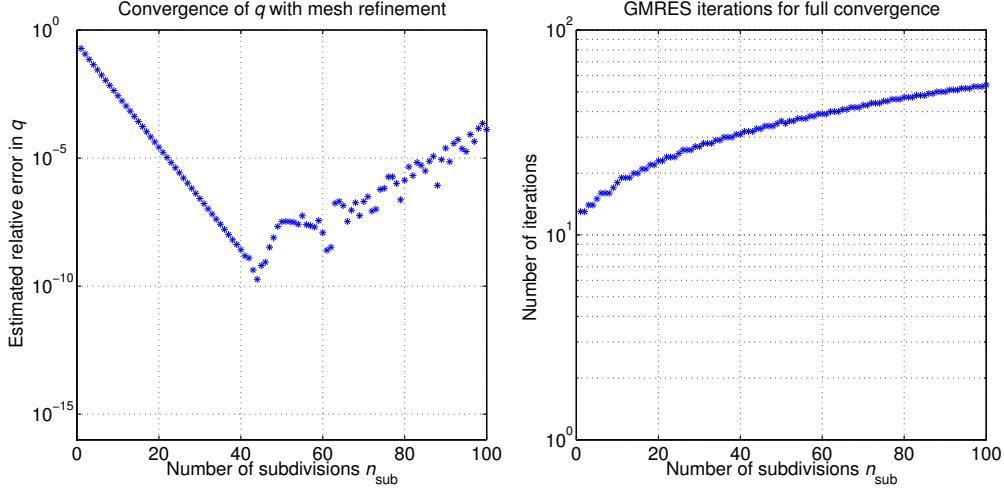


Figure 3: Convergence for  $q$  of (7) using (9) and the program demo1b.m (a loop of demo1.m) with  $\lambda=0.999$ ,  $\theta=\pi/2$ ,  $n_{\text{pan}}=10$ , and  $\text{evec}=1$ . The reference value is  $q = 1.1300163213105365$ . There are  $n_p = 160 + 32n_{\text{sub}}$  unknowns in the main linear system. Left: Convergence with  $n_{\text{sub}}$ . Right: The number of iterations needed to meet an estimated relative residual of  $\epsilon_{\text{mach}}$ .

Here the superscript  $\star$  indicates that only entries of a matrix  $K_{ij}$  whose indices  $i$  and  $j$  correspond to points  $z_i$  and  $z_j$  that both belong to the boundary segment  $\Gamma^\star$  are retained. The remaining entries are zero.

Now we introduce two diagonal matrices  $\mathbf{W}_{\text{coa}}$  and  $\mathbf{W}_{\text{fin}}$  which have the quadrature weights  $w_i$  on the diagonal. Furthermore, we need a prolongation matrix  $\mathbf{P}$  which interpolates functions known at points on the coarse grid to points on the fine grid. The construction of  $\mathbf{P}$  relies on panelwise 15-degree polynomial interpolation in parameter using Vandermonde matrices. We also construct a weighted prolongation matrix  $\mathbf{P}_W$  via

$$\mathbf{P}_W = \mathbf{W}_{\text{fin}} \mathbf{P} \mathbf{W}_{\text{coa}}^{-1}. \quad (14)$$

The matrices  $\mathbf{P}$  and  $\mathbf{P}_W$  share the same sparsity pattern. They are rectangular matrices, similar to the identity matrix, but with one full  $(4 + 2n_{\text{sub}})16 \times 64$  block. Let superscript  $T$  denote the transpose. Then

$$\mathbf{P}_W^T \mathbf{P} = \mathbf{I}_{\text{coa}} \quad (15)$$

holds exactly. See Appendix A and [22, Section 4.3].

Equipped with  $\mathbf{P}$  and  $\mathbf{P}_W$  we are ready to compress (9) on the fine grid to an equation essentially on the coarse grid. This compression is done without the loss of accuracy – the discretization error in the solution is unaffected and no information is lost. The compression relies on the variable substitution

$$(\mathbf{I}_{\text{fin}} + \lambda \mathbf{K}_{\text{fin}}^\star) \boldsymbol{\rho}_{\text{fin}} = \mathbf{P} \tilde{\boldsymbol{\rho}}_{\text{coa}}. \quad (16)$$

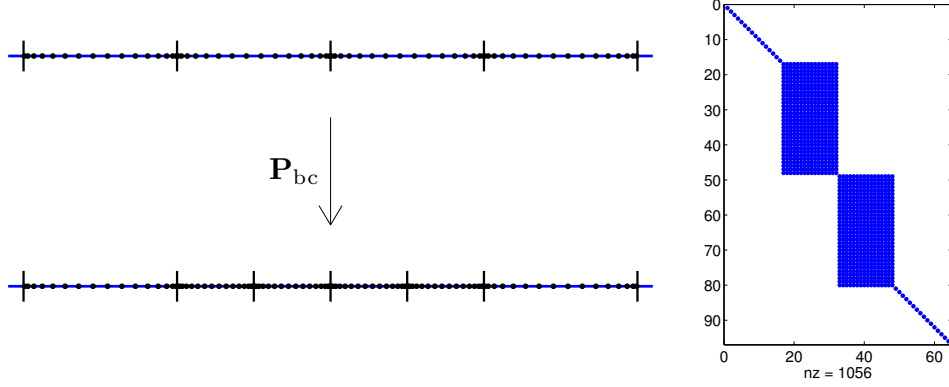


Figure 4: Left: The prolongation operator  $\mathbf{P}_{bc}$  performs panelwise interpolation from a grid on a four-panel mesh to a grid on a six-panel mesh. Right: The sparsity pattern of  $\mathbf{P}_{bc}$ .

Here  $\tilde{\rho}_{coa}$  is the discretization of a piecewise smooth *transformed density*. The compression also uses the low-rank decomposition

$$\mathbf{K}_{fin}^o = \mathbf{P} \mathbf{K}_{coa}^o \mathbf{P}_W^T, \quad (17)$$

which should hold to about machine precision.

The compressed version of (9) reads

$$(\mathbf{I}_{coa} + \lambda \mathbf{K}_{coa}^o \mathbf{R}) \tilde{\rho}_{coa} = \lambda \mathbf{g}_{coa}, \quad (18)$$

where the compressed weighted inverse  $\mathbf{R}$  is given by

$$\mathbf{R} = \mathbf{P}_W^T (\mathbf{I}_{fin} + \lambda \mathbf{K}_{fin}^*)^{-1} \mathbf{P}. \quad (19)$$

See Appendix B for details on the derivation. The compressed weighted inverse  $\mathbf{R}$ , for  $\Gamma$  of (1), is a block diagonal matrix with one full  $64 \times 64$  block and the remaining entries coinciding with those of the identity matrix.

After having solved (18) for  $\tilde{\rho}_{coa}$ , the density  $\rho_{fin}$  can easily be reconstructed from  $\tilde{\rho}_{coa}$  in a post-processor, see Section 9. It is important to observe, however, that  $\rho_{fin}$  is not always needed. For example, the quantity  $q$  of (7) can be computed directly from  $\tilde{\rho}_{coa}$ . Let  $\zeta_{coa}$  be a column vector which contains values of  $|\dot{z}_i|$  multiplied with  $\Re\{\bar{e}z_i\}$ . Then

$$q = \Re\{\zeta_{coa}\}^T \mathbf{W}_{coa} \mathbf{R} \tilde{\rho}_{coa}. \quad (20)$$

See Appendix C for a proof.

## 6 The recursion for $\mathbf{R}$

The compressed weighted inverse  $\mathbf{R}$  is costly to compute from its definition (19). As we saw in Section 4, the inversion of large matrices  $(\mathbf{I} + \mathbf{K})$  on



highly refined grids could also be unstable. Fortunately, the computation of  $\mathbf{R}$  can be greatly sped up and stabilized via a recursion. In [31, Section 7.2] this recursion is derived in a roundabout way and uses a refined grid that differs from that of the present tutorial. A better derivation can be found in [22, Section 5], but there the setting is more general so that text could be hard to follow. Here we focus on results.

## 6.1 Basic prolongation matrices

Let  $\mathbf{P}_{bc}$  be a prolongation matrix, performing panelwise 15-degree polynomial interpolation in parameter from a 64-point grid on a four-panel mesh to a 96-point grid on a six-panel mesh as shown in Figure 4. Let  $\mathbf{P}_{Wbc}$  be a weighted prolongation matrix in the style of (14). If  $\mathbf{T16}$  and  $\mathbf{W16}$  are the nodes and weights of 16-point Gauss–Legendre quadrature on the canonical interval  $[-1, 1]$ , then  $\mathbf{P}_{bc}$  and  $\mathbf{P}_{Wbc}$  can be constructed as

```

T32=[T16-1;T16+1]/2;
W32=[W16;W16]/2;
A=ones(16);
AA=ones(32,16);
for k=2:16
    A(:,k)=A(:,k-1).*T16;
    AA(:,k)=AA(:,k-1).*T32;
end
IP=AA/A;
IPW=IP.*(W32*(1./W16)');
%
Pbc=blkdiag(eye(16),IP,rot90(IP,2),eye(16));
PWbc=blkdiag(eye(16),IPW,rot90(IPW,2),eye(16));

```

See [30, Appendix A] for an explanation of why high-degree polynomial interpolation involving ill-conditioned Vandermonde systems gives accurate results for smooth functions.

## 6.2 Discretization on nested meshes

Let  $\Gamma_i^*$ ,  $i = 1, 2, \dots, n_{\text{sub}}$ , be a sequence of subsets of  $\Gamma^*$  with  $\Gamma_{i-1}^* \subset \Gamma_i^*$  and  $\Gamma_{n_{\text{sub}}}^* = \Gamma^*$ . Let there also be a six-panel mesh and a corresponding 96-point grid on each  $\Gamma_i^*$ . The construction of the subsets and their meshes should be such that if  $z(s)$ ,  $s \in [-2, 2]$ , is a local parameterization of  $\Gamma_i^*$ , then the breakpoints (locations of panel endpoints) of its mesh are at  $s \in \{-2, -1, -0.5, 0, 0.5, 1, 2\}$  and the breakpoints of the mesh on  $\Gamma_{i-1}^*$  are at  $s \in \{-1, -0.5, -0.25, 0, -0.25, 0.5, 1\}$ . We denote this type of nested six-panel meshes *type b*. The index  $i$  is the *level*. An example of a sequence

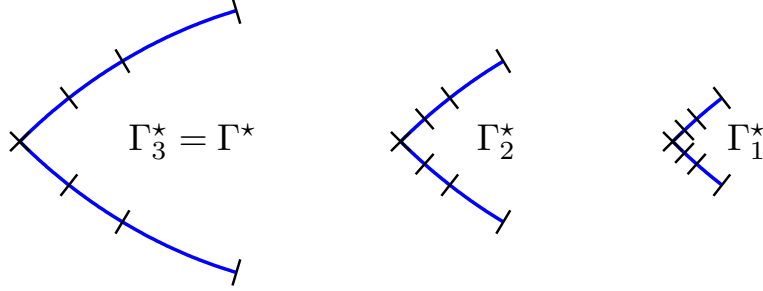


Figure 5: The boundary subsets  $\Gamma_3^*$ ,  $\Gamma_2^*$ , and  $\Gamma_1^*$  along with their corresponding type **b** meshes for  $n_{\text{sub}} = 3$ .

of subsets and type **b** meshes on  $\Gamma^*$  is shown in Figure 5 for  $n_{\text{sub}} = 3$ . Compare [21, Figure 2] and [22, Figure 5.1].

Let  $\mathbf{K}_{ib}$  denote the discretization of  $K$  on a type **b** mesh on  $\Gamma_i^*$ . In the spirit of (12,13) we write

$$\mathbf{K}_{ib} = \mathbf{K}_{ib}^* + \mathbf{K}_{ib}^\circ, \quad (21)$$

where the superscript  $\star$  indicates that only entries with both indices corresponding to points on the four inner panels are retained.

### 6.3 The recursion proper

Now, let  $\mathbf{R}_{n_{\text{sub}}}$  denote the full  $64 \times 64$  diagonal block of  $\mathbf{R}$ . The recursion for  $\mathbf{R}_{n_{\text{sub}}}$  is derived in Appendix D and it reads

$$\mathbf{R}_i = \mathbf{P}_{Wbc}^T (\mathbb{F}\{\mathbf{R}_{i-1}^{-1}\} + \mathbf{I}_b^\circ + \lambda \mathbf{K}_{ib}^\circ)^{-1} \mathbf{P}_{bc}, \quad i = 1, \dots, n_{\text{sub}}, \quad (22)$$

$$\mathbb{F}\{\mathbf{R}_0^{-1}\} = \mathbf{I}_b^* + \lambda \mathbf{K}_{1b}^*, \quad (23)$$

where the operator  $\mathbb{F}\{\cdot\}$  expands its matrix argument by zero-padding (adding a frame of zeros of width 16 around it). Note that the initializer  $\mathbf{R}_0$  of (23) makes the recursion (22) take the first step

$$\mathbf{R}_1 = \mathbf{P}_{Wbc}^T (\mathbf{I}_b + \lambda \mathbf{K}_{1b})^{-1} \mathbf{P}_{bc}.$$

The program `demo2.m` sets up the linear system (18), runs the recursion (22,23), and solves the linear system using the same techniques as `demo1.m`, see Section 4. In fact, the results produced by the two programs are very similar, at least up to  $n_{\text{sub}} = 40$ . This supports the claim of Section 5 that the discretization error in the solution is unaffected by compression.

Figure 6 demonstrates the power of RCIP: fewer unknowns and faster execution, better conditioning (the number of GMRES iterations does not grow), and higher achievable accuracy. Compare Figure 3. We emphasize that the number  $n_{\text{sub}}$  of recursion steps (levels) used in (22) corresponds to the number of subdivisions  $n_{\text{sub}}$  used to construct the fine mesh.

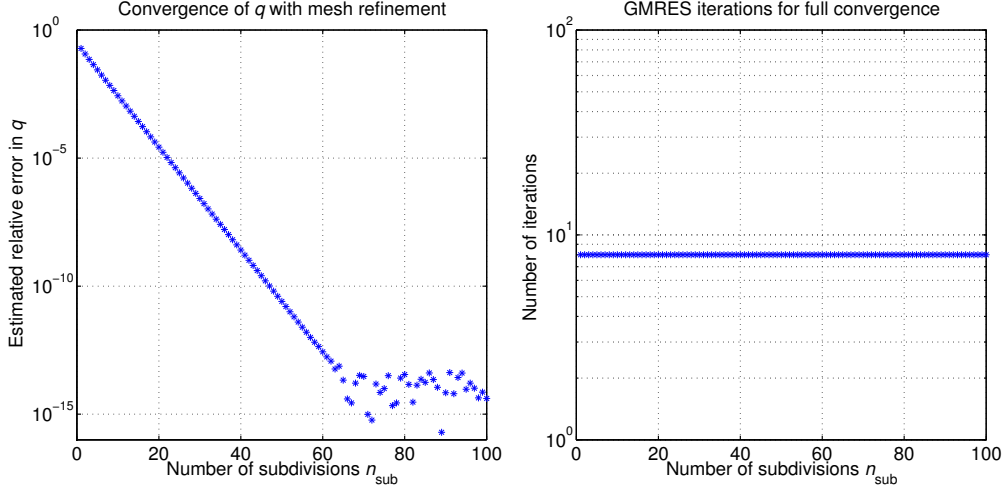


Figure 6: Same as Figure 3, but using (18) and the program `demo2b.m` (a loop of `demo2.m`). There are only  $n_p = 160$  unknowns in the main linear system.

## 7 Schur–Banachiewicz speedup of the recursion

The recursion (22) can be sped up using the Schur–Banachiewicz inverse formula for partitioned matrices [36], which in this context can be written [32, Appendix B]

$$\begin{bmatrix} \mathbf{P}_W^{*T} & \mathbf{0} \\ \mathbf{0} & \mathbf{I} \end{bmatrix} \begin{bmatrix} \mathbf{A}^{-1} & \mathbf{U} \\ \mathbf{V} & \mathbf{D} \end{bmatrix}^{-1} \begin{bmatrix} \mathbf{P}^* & \mathbf{0} \\ \mathbf{0} & \mathbf{I} \end{bmatrix} = \begin{bmatrix} \mathbf{P}_W^{*T} \mathbf{A} \mathbf{P}^* + \mathbf{P}_W^{*T} \mathbf{A} \mathbf{U} (\mathbf{D} - \mathbf{V} \mathbf{A} \mathbf{U})^{-1} \mathbf{V} \mathbf{A} \mathbf{P}^* & -\mathbf{P}_W^{*T} \mathbf{A} \mathbf{U} (\mathbf{D} - \mathbf{V} \mathbf{A} \mathbf{U})^{-1} \\ -(\mathbf{D} - \mathbf{V} \mathbf{A} \mathbf{U})^{-1} \mathbf{V} \mathbf{A} \mathbf{P}^* & (\mathbf{D} - \mathbf{V} \mathbf{A} \mathbf{U})^{-1} \end{bmatrix}, \quad (24)$$

where  $\mathbf{A}$  plays the role of  $\mathbf{R}_{i-1}$ ,  $\mathbf{P}^*$  and  $\mathbf{P}_W^*$  are submatrices of  $\mathbf{P}_{bc}$  and  $\mathbf{P}_{Wbc}$ , and  $\mathbf{U}$ ,  $\mathbf{V}$ , and  $\mathbf{D}$  refer to blocks of  $\mathbf{I}_b^\circ + \lambda \mathbf{K}_{ib}^\circ$ .

The program `demo3.m` is based on `demo2.m`, but has (24) incorporated. Besides, the integral equation (3) is replaced with

$$\rho(r) + 2\lambda \int_{\Gamma} \frac{\partial G}{\partial \nu}(r, r') \rho(r') d\ell' + \int_{\Gamma} \rho(r') d\ell' = 2\lambda (e \cdot \nu), \quad r \in \Gamma, \quad (25)$$

which has the same solution  $\rho(r)$  but is more stable for  $\lambda$  close to one. For the discretization of (25) to fit the form (18), the last term on the left hand side of (25) is added to the matrix  $\lambda \mathbf{K}_{coa}^\circ$  of (18).

The execution of `demo3.m` is faster than that of `demo2.m`. Figure 7 shows that a couple of extra digits are gained by using (25) rather than (3) and that full machine accuracy is achieved for  $n_{sub} > 60$ .

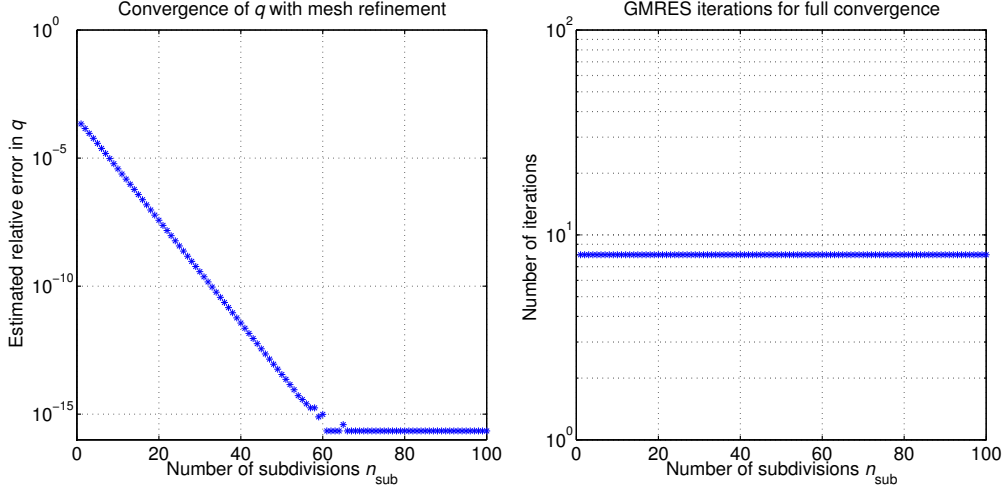


Figure 7: Same as Figure 6, but the program `demo3b.m` is used.

## 8 Various useful quantities

Let us introduce a new discrete density  $\hat{\rho}_{\text{coa}}$  via

$$\hat{\rho}_{\text{coa}} = \mathbf{R} \tilde{\rho}_{\text{coa}}. \quad (26)$$

Rewriting (18) in terms of  $\hat{\rho}_{\text{coa}}$  gives

$$(\mathbf{R}^{-1} + \lambda \mathbf{K}_{\text{coa}}^{\circ}) \hat{\rho}_{\text{coa}} = \lambda \mathbf{g}_{\text{coa}}, \quad (27)$$

which resembles the original equation (8). We see that  $\mathbf{K}_{\text{coa}}^{\circ}$ , which is discretized using Gauss–Legendre quadrature, acts on  $\hat{\rho}_{\text{coa}}$ . Therefore one can interpret  $\hat{\rho}_{\text{coa}}$  as pointwise values of the original density  $\rho(r)$ , multiplied with weight corrections suitable for integration against polynomials. We refer to  $\hat{\rho}_{\text{coa}}$  as a *weight-corrected density*. See, further, Appendix C.

Assume now that there is a square matrix  $\mathbf{S}$  which maps  $\tilde{\rho}_{\text{coa}}$  to discrete values  $\rho_{\text{coa}}$  of the original density on the coarse grid

$$\rho_{\text{coa}} = \mathbf{S} \tilde{\rho}_{\text{coa}}. \quad (28)$$

The matrix  $\mathbf{S}$  allows us to rewrite (18) as a system for the original density

$$(\mathbf{S}^{-1} + \lambda \mathbf{K}_{\text{coa}}^{\circ} \mathbf{R} \mathbf{S}^{-1}) \rho_{\text{coa}} = \lambda \mathbf{g}_{\text{coa}}. \quad (29)$$

We can interpret the composition  $\mathbf{R} \mathbf{S}^{-1}$  as a matrix of multiplicative weight corrections that compensate for the singular behavior of  $\rho(r)$  on  $\Gamma^*$  when Gauss–Legendre quadrature is used.

Let  $\mathbf{Y}$  denote the rectangular matrix

$$\mathbf{Y} = (\mathbf{I}_{\text{fin}} + \lambda \mathbf{K}_{\text{fin}}^{\star})^{-1} \mathbf{P}, \quad (30)$$

and let  $\mathbf{Q}$  be a restriction operator which performs panelwise 15-degree polynomial interpolation in parameter from a grid on the fine mesh to a grid on the coarse mesh. We see from (16) that  $\mathbf{Y}$  is the mapping from  $\tilde{\boldsymbol{\rho}}_{\text{coa}}$  to  $\boldsymbol{\rho}_{\text{fin}}$ . Therefore the columns of  $\mathbf{Y}$  can be interpreted as discrete basis functions for  $\rho(r)$ . It holds by definition that

$$\mathbf{Q}\mathbf{P} = \mathbf{I}_{\text{coa}}, \quad (31)$$

$$\mathbf{Q}\mathbf{Y} = \mathbf{S}. \quad (32)$$

The quantities and interpretations of this section come in handy in various situations, for example in 3D extensions of the RCIP method [33]. An efficient scheme for constructing  $\mathbf{S}$  will be presented in Section 10.

## 9 Reconstruction of $\boldsymbol{\rho}_{\text{fin}}$ from $\tilde{\boldsymbol{\rho}}_{\text{coa}}$

The action of  $\mathbf{Y}$  on  $\tilde{\boldsymbol{\rho}}_{\text{coa}}$ , which gives  $\boldsymbol{\rho}_{\text{fin}}$ , can be obtained by, in a sense, running the recursion (22) backwards. The process is described in detail in [21, Section 7]. Here we focus on results.

The backward recursion on  $\Gamma^*$  reads

$$\tilde{\boldsymbol{\rho}}_{\text{coa},i} = \left[ \mathbf{I}_{\text{b}} - \lambda \mathbf{K}_{\text{ib}}^{\circ} \left( \mathbb{F}\{\mathbf{R}_{i-1}^{-1}\} + \mathbf{I}_{\text{b}}^{\circ} + \lambda \mathbf{K}_{\text{ib}}^{\circ} \right)^{-1} \right] \mathbf{P}_{\text{bc}} \tilde{\boldsymbol{\rho}}_{\text{coa},i}, \quad i = n_{\text{sub}}, \dots, 1. \quad (33)$$

Here  $\tilde{\boldsymbol{\rho}}_{\text{coa},i}$  is a column vector with 64 elements. In particular,  $\tilde{\boldsymbol{\rho}}_{\text{coa},n_{\text{sub}}}$  is the restriction of  $\tilde{\boldsymbol{\rho}}_{\text{coa}}$  to  $\Gamma^*$ , while  $\tilde{\boldsymbol{\rho}}_{\text{coa},i}$  are taken as elements  $\{17 : 80\}$  of  $\tilde{\boldsymbol{\rho}}_{\text{coa},i+1}$  for  $i < n_{\text{sub}}$ . The elements  $\{1 : 16\}$  and  $\{81 : 96\}$  of  $\tilde{\boldsymbol{\rho}}_{\text{coa},i}$  are the reconstructed values of  $\boldsymbol{\rho}_{\text{fin}}$  on the outermost panels of a type **b** mesh on  $\Gamma_i^*$ . Outside of  $\Gamma^*$ ,  $\boldsymbol{\rho}_{\text{fin}}$  coincides with  $\tilde{\boldsymbol{\rho}}_{\text{coa}}$ .

When the recursion is completed, the reconstructed values of  $\boldsymbol{\rho}_{\text{fin}}$  on the four innermost panels are obtained from

$$\mathbf{R}_0 \tilde{\boldsymbol{\rho}}_{\text{coa},0}. \quad (34)$$

Should one wish to interrupt the recursion (33) prematurely, at step  $i = j$  say, then

$$\mathbf{R}_{j-1} \tilde{\boldsymbol{\rho}}_{\text{coa},(j-1)} \quad (35)$$

gives values of a weight-corrected density on the four innermost panels of a type **b** mesh on  $\Gamma_j^*$ . That is, we have a part-way reconstructed weight-corrected density  $\hat{\boldsymbol{\rho}}_{\text{part}}$  on a mesh that is  $n_{\text{sub}} - j + 1$  times refined. This observation is useful in the context of evaluating layer potentials close to their sources.

If the memory permits, one can store the matrices  $\mathbf{K}_{\text{ib}}^{\circ}$  and  $\mathbf{R}_i$  in the forward recursion (22) and reuse them in the backward recursion (33). Otherwise they may be computed afresh.

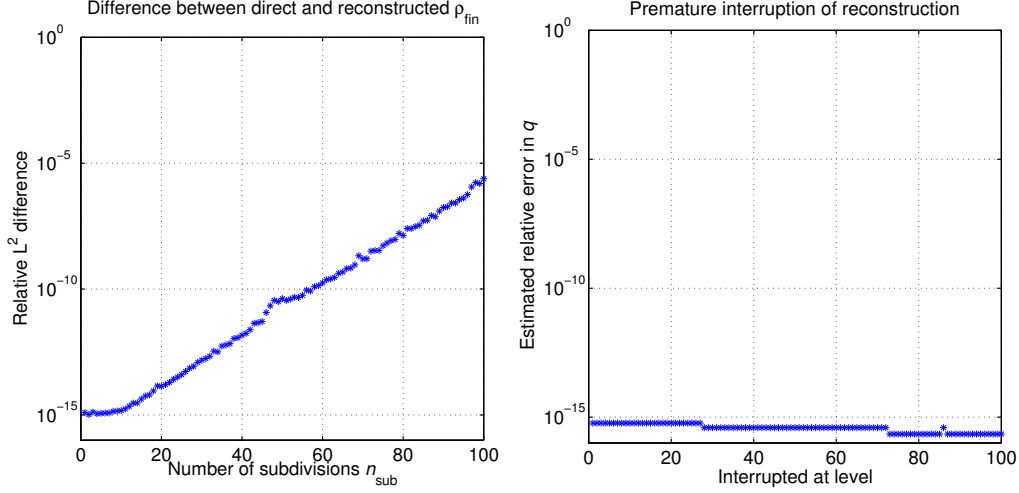


Figure 8: Output from `demo4.m` and `demo5.m`. Left: A comparison of  $\rho_{\text{fin}}$  from the unstable equation (9) and  $\rho_{\text{fin}}$  reconstructed from  $\tilde{\rho}_{\text{coa}}$  of (18) via (33). Right: Relative accuracy in  $q$  of (7) from part-way reconstructed solutions  $\hat{\rho}_{\text{part}}$ .

The program `demo4.m` builds on the program `demo3.m`, using (18) for (25). After the main linear system is solved for  $\tilde{\rho}_{\text{coa}}$ , a postprocessor reconstructs  $\rho_{\text{fin}}$  via (33). Then a comparison is made with a solution  $\rho_{\text{fin}}$  obtained by solving the un-compressed system (9). Figure 8 shows that for  $n_{\text{sub}} < 10$  the results are virtually identical. This verifies the correctness of (33). For  $n_{\text{sub}} > 10$  the result start to deviate. That illustrates the instabilities associated with solving (9) on a highly refined mesh. Compare Figure 3.

The program `demo5.m` investigates the effects of premature interruption of (33). The number of recursion steps is set to  $n_{\text{sub}} = 100$  and the recursion is interrupted at different levels. The density  $\rho_{\text{fin}}$  is reconstructed on outer panels down to the level of interruption. Then a weight-corrected density is produced at the innermost four panels according to (35). Finally  $q$  of (7) is computed from this part-way reconstructed solution. The right image of Figure 8 shows that the quality of  $q$  is unaffected by the level of interruption.

## 10 The construction of $\mathbf{S}$

This section discusses the construction of  $\mathbf{S}$  and other auxiliary matrices. Note that in many applications, these matrices are not needed.

The entries of the matrices  $\mathbf{P}$ ,  $\mathbf{P}_W$ ,  $\mathbf{Q}$ ,  $\mathbf{R}$ ,  $\mathbf{S}$ , and  $\mathbf{Y}$  can only differ from those of the identity matrix when both indices correspond to discretization points on  $\Gamma^*$ . For example, the entries of  $\mathbf{R}$  only differ from the identity matrix for the  $64 \times 64$  block denoted  $\mathbf{R}_{n_{\text{sub}}}$  in (22). In accordance with this notation we introduce  $\mathbf{P}_{n_{\text{sub}}}$ ,  $\mathbf{P}_{Wn_{\text{sub}}}$ ,  $\mathbf{Q}_{n_{\text{sub}}}$ ,  $\mathbf{S}_{n_{\text{sub}}}$  and  $\mathbf{Y}_{n_{\text{sub}}}$  for the

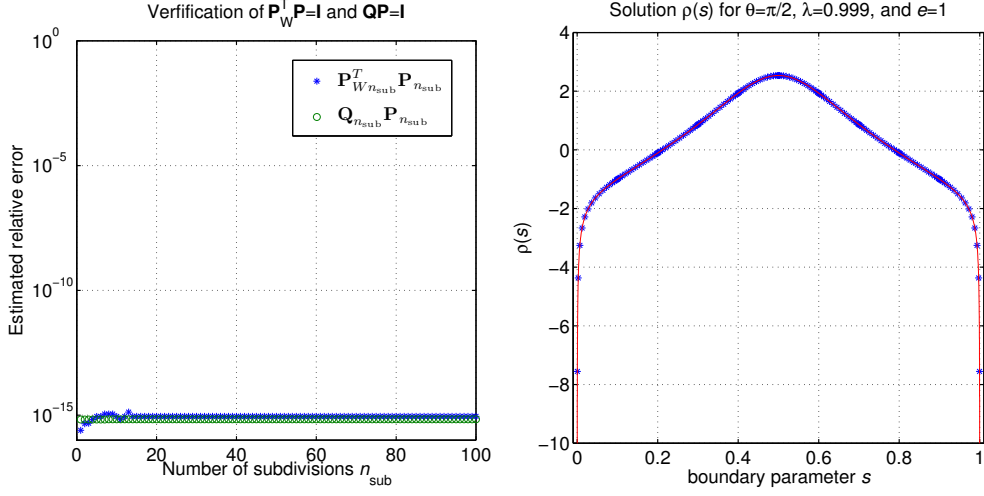


Figure 9: Left: The identities (15) and (31) hold to high accuracy in our implementation, irrespective of the degree of mesh refinement. Right: The solution  $\rho$  to (25) on (1) with parameters as specified in Section 4. The solution with RCIP (18) and (28), shown as blue stars, agrees with the solution from (9), shown as a red solid line. The solution diverges in the corner.

restriction of  $\mathbf{P}$ ,  $\mathbf{P}_W$ ,  $\mathbf{Q}$ ,  $\mathbf{S}$  and  $\mathbf{Y}$  to  $\Gamma^*$ . In the codes of this section we often use this restricted type of matrices, leaving the identity part out.

We observe that  $\mathbf{S}_{n_{\text{sub}}}$  is a square  $64 \times 64$  matrix;  $\mathbf{P}_{n_{\text{sub}}}$ ,  $\mathbf{P}_{W n_{\text{sub}}}$  and  $\mathbf{Y}_{n_{\text{sub}}}$  are rectangular  $16(4 + 2n_{\text{sub}}) \times 64$  matrices; and  $\mathbf{Q}_{n_{\text{sub}}}$  is a rectangular  $64 \times 16(4 + 2n_{\text{sub}})$  matrix. Furthermore,  $\mathbf{Q}_{n_{\text{sub}}}$  is very sparse for large  $n_{\text{sub}}$ . All columns of  $\mathbf{Q}_{n_{\text{sub}}}$  with column indices corresponding to points on panels that result from more than eight subdivisions are identically zero.

The program `demo6.m` sets up  $\mathbf{P}_{n_{\text{sub}}}$ ,  $\mathbf{P}_{W n_{\text{sub}}}$  and  $\mathbf{Q}_{n_{\text{sub}}}$ , shows their sparsity patterns, and verifies the identities (15) and (31). The implementations for  $\mathbf{P}_{n_{\text{sub}}}$  and  $\mathbf{P}_{W n_{\text{sub}}}$  rely on repeated interpolation from coarser to finer intermediate grids. The implementation of  $\mathbf{Q}_{n_{\text{sub}}}$  relies on keeping track of the relation between points on the original coarse and fine grids. Output from `demo6.m` is depicted in the left image of Figure 9. Note that the matrices  $\mathbf{P}_{n_{\text{sub}}}$  and  $\mathbf{P}_{W n_{\text{sub}}}$  are never needed in applications.

We are now ready to construct  $\mathbf{S}$ . Section 9 presented a scheme for evaluating the action of  $\mathbf{Y}_{n_{\text{sub}}}$  on discrete functions on the coarse grid on  $\Gamma^*$ . The matrix  $\mathbf{Y}_{n_{\text{sub}}}$ , itself, can be constructed by applying this scheme to a  $64 \times 64$  identity matrix. The matrix  $\mathbf{Q}_{n_{\text{sub}}}$  was set up in `demo6.m`. Composing these two matrices gives  $\mathbf{S}_{n_{\text{sub}}}$ , see (32). This is done in the program `demo7.m`, where the identity part is added as to get the entire matrix  $\mathbf{S}$ . In previous work on RCIP we have found use for  $\mathbf{S}$  in complex situations where (29) is preferable over (18), see [33, Section 9]. If one merely needs  $\rho_{\text{coa}}$  from  $\tilde{\rho}_{\text{coa}}$  in a post-processor, setting up  $\mathbf{S}$  and using (28) is not

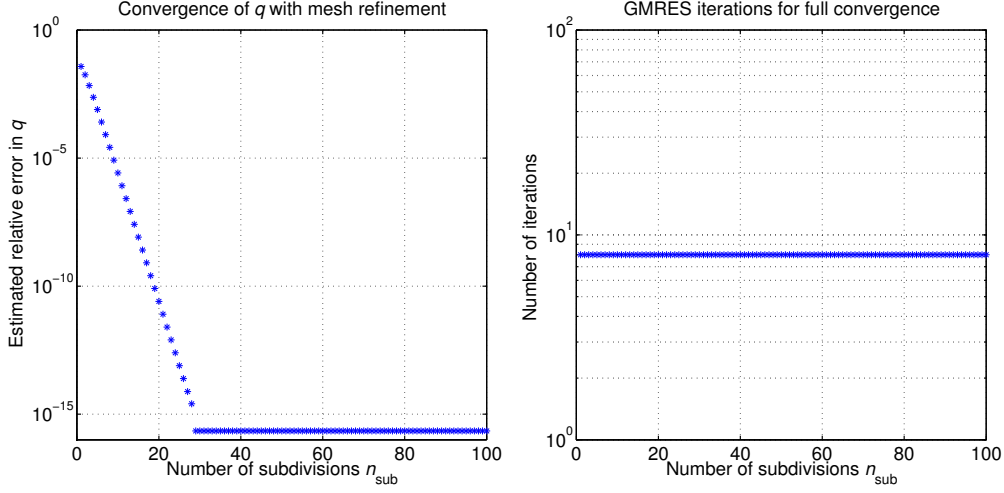


Figure 10: Same as Figure 7, but the program `demo8b.m` is used.

worthwhile. It is cheaper to let  $\mathbf{Y}$  act on  $\tilde{\rho}_{\text{coa}}$  and then let  $\mathbf{Q}$  act on the resulting vector. Anyhow, `demo7.m` builds on `demo4.m` and gives as output  $\rho_{\text{coa}}$  computed via (28), see the right image of Figure 9. For comparison,  $\rho_{\text{fin}}$ , computed from (9), is also shown.

## 11 Initiating $\mathbf{R}$ using fixed-point iteration

It often happens that  $\Gamma_i^*$  is wedge-like. A corner of a polygon, for example, has wedge-like  $\Gamma_i^*$  at all levels. If  $\Gamma^*$  is merely piecewise smooth, then the  $\Gamma_i^*$  are wedge-like to double precision accuracy for  $n_{\text{sub}} - i \gg 1$ .

Wedge-like sequences of  $\Gamma_i^*$  open up for simplifications and speedup in the recursion (22,23). Particularly so if the kernel of the integral operator  $K$  of (6) is scale invariant on wedges. Then the matrix  $\mathbf{K}_{ib}^o$  becomes independent of  $i$ . It can be denoted by  $\mathbf{K}_b^o$  and needs only to be constructed once. Furthermore, the recursion (22,23) assumes the form of a fixed-point iteration

$$\mathbf{R}_i = \mathbf{P}_{W_{bc}}^T (\mathbb{F}\{\mathbf{R}_{i-1}^{-1}\} + \mathbf{I}_b^o + \lambda \mathbf{K}_b^o)^{-1} \mathbf{P}_{bc}, \quad i = 1, \dots \quad (36)$$

$$\mathbb{F}\{\mathbf{R}_0^{-1}\} = \mathbf{I}_b^* + \lambda \mathbf{K}_b^*. \quad (37)$$

The iteration (36) can be run until  $\mathbf{R}_i$  reaches its converged value  $\mathbf{R}_*$ . One need not know in advance how many iterations this takes. Choosing the number  $n_{\text{sub}}$  of levels needed, in order to meet a beforehand given tolerance in  $\mathbf{R}_{n_{\text{sub}}}$ , is otherwise a problem in connection with (22,23) and non-wedge-like  $\Gamma^*$ . This number has no general upper bound.

Assume now that the kernel of  $K$  is scale invariant on wedges. If all  $\Gamma_i^*$  are wedge-like, then (36,37) replaces (22,23) entirely. If  $\Gamma^*$  is merely piecewise



smooth, then (36,37) can be run on a wedge with the same opening angle as  $\Gamma^*$ , to produce an initializer to (22). That initializer could often be more appropriate than  $\mathbf{R}_0$  of (23), which is plagued with a very large discretization error whenever (11) is used. The fixed-point initializer  $\mathbf{R}_*$  is implemented in the program `demo8b.m`, which is an upgrading of `demo3b.m`, and produces Figure 10. A comparison of Figure 10 with Figure 7 shows that the number  $n_{\text{sub}}$  of levels needed for full convergence with the initializer  $\mathbf{R}_*$  is halved compared to when using the initializer  $\mathbf{R}_0$  of (23).

There are, generally speaking, several advantages with using the initializer  $\mathbf{R}_*$ , rather than  $\mathbf{R}_0$  of (23), in (22) on a non-wedge-like  $\Gamma^*$ : First, the number of different matrices  $\mathbf{R}_i$  and  $\mathbf{K}_{ib}^\circ$  needed in (22) and in (33) is reduced as the recursions are shortened. This means savings in storage. Second, the number  $n_{\text{sub}}$  of levels needed for full convergence in (22) seems to always be bounded. The hard work is done in (36). Third, Newton's method can be used to accelerate (36). That is the topic of Section 12.

## 12 Newton acceleration

When solving integral equations stemming from particularly challenging elliptic boundary value problems with solutions  $\rho(r)$  that are barely absolutely integrable, the fixed-point iteration (36,37) on wedge-like  $\Gamma^*$  may need a very large number of steps to reach full convergence. See [24, Section 6.3] for an example where  $2 \cdot 10^5$  steps are needed.

Fortunately, (36) can be cast as a non-linear matrix equation

$$\mathbf{G}(\mathbf{R}_*) \equiv \mathbf{P}_{Wbc}^T \mathbf{A}(\mathbf{R}_*) \mathbf{P}_{bc} - \mathbf{R}_* = 0, \quad (38)$$

where  $\mathbf{R}_*$ , as in Section 11, is the fixed-point solution and

$$\mathbf{A}(\mathbf{R}_*) = (\mathbb{F}\{\mathbf{R}_*^{-1}\} + \mathbf{I}_b^\circ + \lambda \mathbf{K}_b^\circ)^{-1}. \quad (39)$$

The non-linear equation (38), in turn, can be solved for  $\mathbf{R}_*$  with a variant of Newton's method. Let  $\mathbf{X}$  be a matrix-valued perturbation of  $\mathbf{R}_*$  and expand  $\mathbf{G}(\mathbf{R}_* + \mathbf{X}) = 0$  to first order in  $\mathbf{X}$ . This gives a Sylvester-type matrix equation

$$\mathbf{X} - \mathbf{P}_{Wbc}^T \mathbf{A}(\mathbf{R}_*) \mathbb{F}\{\mathbf{R}_*^{-1} \mathbf{X} \mathbf{R}_*^{-1}\} \mathbf{A}(\mathbf{R}_*) \mathbf{P}_{bc} = \mathbf{G}(\mathbf{R}_*) \quad (40)$$

for the Newton update  $\mathbf{X}$ . One can use the MATLAB built-in function `dlyap` for (40), but GMRES seems to be more efficient and we use that method. Compare [24, Section 6.2].

Figure 11 shows a comparison between the fixed-point iteration (36,37) and Newton's method for computing the fixed-point solution  $\mathbf{R}_*$  to (38) on a wedge-like  $\Gamma^*$ . The program `demo9.m` is used and it incorporates Schur–Banachiewicz speedup in the style of Section 7. The wedge opening angle

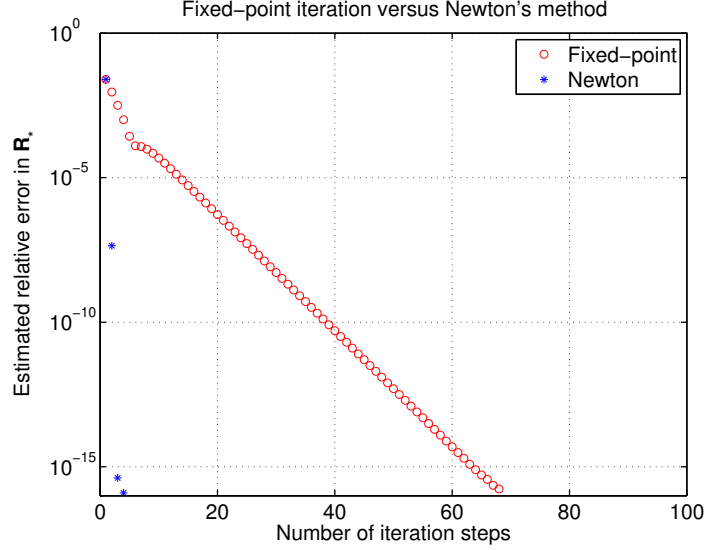


Figure 11: Output from the program `demo9.m`. The fixed-point iteration (36,37) is compared to Newton's method for (38).

is  $\theta = \pi/2$ , The integral operator  $K$  is the same as in (6), and  $\lambda = 0.999$ . The relative difference between the two converged solutions  $\mathbf{R}_*$  is  $5 \cdot 10^{-16}$ . Figure 11 clearly shows that (36,37) converges linearly (in 68 iterations), while Newton's method has quadratic convergence. Only four iterations are needed. The computational cost per iteration is, of course, higher for Newton's method than for the fixed-point iteration, but it is the same at each step. Recall that the size of the underlying matrix  $\mathbf{I}_{\text{fin}} + \lambda \mathbf{K}_{\text{fin}}^*$ , that is inverted according to (19), grows linearly with the number of steps needed in the fixed-point iteration. This example therefore demonstrates that one can invert and compress a linear system of the type (19) in sub-linear time.

### 13 The asymptotics of $\rho(r)$ in the corner

The recursion (33) provides a powerful tool for computing the asymptotics of  $\rho(r)$  close to the corner vertex: Deep in the corner, for large  $n_{\text{sub}}$  and small  $i$ , the matrices  $\mathbf{R}_{i-1}$  and  $\mathbf{K}_{ib}^{\circ}$  can be replaced with their asymptotic counterparts  $\mathbf{R}_*$  and  $\mathbf{K}_b^{\circ}$ , see Section 11, so that (33) reads

$$\vec{\rho}_{\text{coa},i} = \mathbf{C} \vec{\rho}_{\text{coa},i}, \quad i = n_{\text{asm}}, \dots, 1, \quad n_{\text{sub}} - n_{\text{asm}} \gg 1, \quad (41)$$

where  $\mathbf{C}$  is the constant  $96 \times 64$  matrix

$$\mathbf{C} = \left[ \mathbf{I}_b - \lambda \mathbf{K}_b^{\circ} (\mathbb{F}\{\mathbf{R}_*^{-1}\} + \mathbf{I}_b^{\circ} + \lambda \mathbf{K}_b^{\circ})^{-1} \right] \mathbf{P}_{\text{bc}}. \quad (42)$$

Each step in (41) reconstructs  $\rho(r)$  on the outermost panels of a mesh on a subset  $\Gamma_i^*$  that is half the size of the subset  $\Gamma_{i+1}^*$  in the previous step.

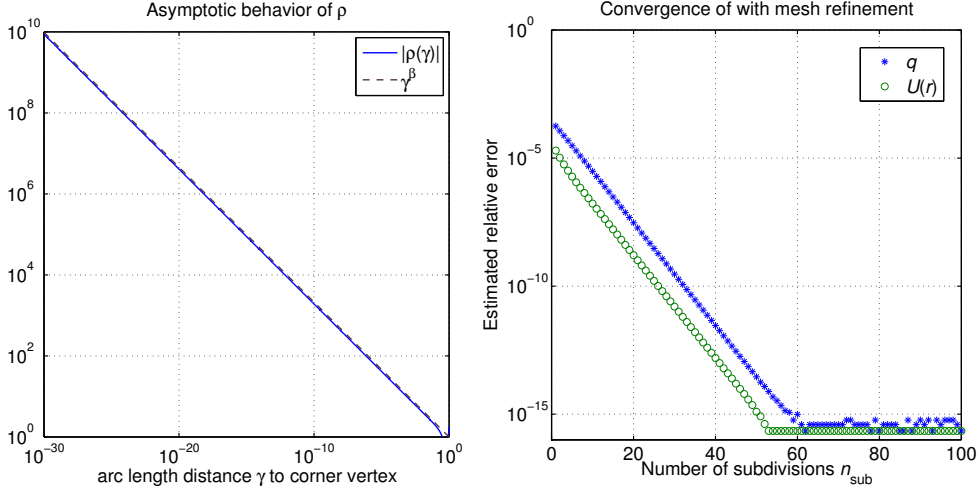


Figure 12: Left:  $\rho(\gamma)$  from `demo8c.m` compared to the asymptotic behavior  $\gamma^\beta$  with  $\beta$  from (44). Right: similar as in Figure 7, but from `demo3c.m` and with `npan=14`. The potential  $U(r)$  at  $r = (0.4, 0.1)$  is evaluated via (45).

Furthermore, the evolution of  $\tilde{\rho}_{\text{coa},i}$  is determined by power iteration applied to a submatrix of  $\mathbf{C}$  given by row indices  $\{17 : 80\}$  and all columns. We denoted this submatrix by  $\mathbf{C}^*$ . The eigenvalues of  $\mathbf{C}^*$  control the behavior of  $\rho(r)$  as the distance to the corner vertex is halved. In particular, if  $\gamma$  is the arc length distance to the vertex then the leading asymptotic behavior is  $\rho(\gamma) \propto \gamma^\beta$  with

$$\beta = -\log_2(d_{\max}), \quad (43)$$

where  $d_{\max}$  is the largest eigenvalue in modulus of  $\mathbf{C}^*$ .

For the opening angle  $\theta = \pi/2$  in the model problem of Section 3 it is possible to derive the closed-form expression [29, Eq. (13)]

$$\beta = \frac{2}{\pi} \arccos\left(\frac{\lambda}{2}\right) - 1. \quad (44)$$

The program `demo8c.m` compares  $\beta$  computed from (43) to  $\beta$  from (44) with  $\lambda = 0.999$ . The relative difference is a mere  $7 \cdot 10^{-16}$ , which means that RCIP provides a competitive alternative to traditional techniques, such as separation of variables [20, Section 2], also for asymptotic studies. The left image of Figure 12 shows the asymptotic behavior of  $\rho(\gamma)$  in the corner.

## 14 On the accuracy of “the solution”

The integral equation (3) comes from a boundary value problem for Laplace’s equation where the potential field  $U(r)$  at a point  $r$  in the plane is related

to  $\rho(r)$  via

$$U(r) = (e \cdot r) - \int_{\Gamma} G(r, r') \rho(r') d\ell', \quad (45)$$

see [31, Section 2.1]. The right image of Figure 12 shows how  $U(r)$  converges with mesh refinement at a point  $r = (0.4, 0.1)$  inside the contour  $\Gamma$ . We see that the accuracy in  $U(r)$  is slightly better than the accuracy of the dipole moment  $q$  of (7). One can say that measuring the field error at a point some distance away from the corner is more forgiving than measuring the dipole moment error. It is possible to construct examples where the difference in accuracy between field solutions and moments of layer densities are more pronounced and this raises the question of how the accuracy of integral equation solvers best should be measured.

## 15 Composed integral operators

Assume that we have a modification of (6) which reads

$$(I + MK) \rho_1(r) = g(r), \quad z \in \Gamma. \quad (46)$$

Here  $K$  and  $g$  are as in (6),  $M$  is a new, bounded, integral operator, and  $\rho_1$  is an unknown layer density to be solved for. This section shows how to apply RCIP to (46) using a simplified version of the scheme in [22].

Let us, temporarily, expand (46) into a system of equations by introducing a new layer density  $\rho_2(r) = K\rho_1(r)$ . Then

$$\rho_1(r) + M\rho_2(r) = g(r), \quad (47)$$

$$-K\rho_1(r) + \rho_2(r) = 0, \quad (48)$$

and after discretization on the fine mesh

$$\left( \begin{bmatrix} \mathbf{I}_{\text{fin}} & \mathbf{0}_{\text{fin}} \\ \mathbf{0}_{\text{fin}} & \mathbf{I}_{\text{fin}} \end{bmatrix} + \begin{bmatrix} \mathbf{0}_{\text{fin}} & \mathbf{M}_{\text{fin}} \\ -\mathbf{K}_{\text{fin}} & \mathbf{0}_{\text{fin}} \end{bmatrix} \right) \begin{bmatrix} \boldsymbol{\rho}_{1\text{fin}} \\ \boldsymbol{\rho}_{2\text{fin}} \end{bmatrix} = \begin{bmatrix} \mathbf{g}_{\text{fin}} \\ 0 \end{bmatrix}. \quad (49)$$

Standard RCIP gives

$$\left( \begin{bmatrix} \mathbf{I}_{\text{coa}} & \mathbf{0}_{\text{coa}} \\ \mathbf{0}_{\text{coa}} & \mathbf{I}_{\text{coa}} \end{bmatrix} + \begin{bmatrix} \mathbf{0}_{\text{coa}} & \mathbf{M}_{\text{coa}}^{\circ} \\ -\mathbf{K}_{\text{coa}}^{\circ} & \mathbf{0}_{\text{coa}} \end{bmatrix} \begin{bmatrix} \mathbf{R}_1 & \mathbf{R}_3 \\ \mathbf{R}_2 & \mathbf{R}_4 \end{bmatrix} \right) \begin{bmatrix} \tilde{\boldsymbol{\rho}}_{1\text{coa}} \\ \tilde{\boldsymbol{\rho}}_{2\text{coa}} \end{bmatrix} = \begin{bmatrix} \mathbf{g}_{\text{coa}} \\ 0 \end{bmatrix}, \quad (50)$$

where the compressed inverse  $\mathbf{R}$  is partitioned into four equi-sized blocks.

Now we replace  $\tilde{\boldsymbol{\rho}}_{1\text{coa}}$  and  $\tilde{\boldsymbol{\rho}}_{2\text{coa}}$  with a single unknown  $\tilde{\boldsymbol{\rho}}_{\text{coa}}$  via

$$\tilde{\boldsymbol{\rho}}_{1\text{coa}} = \tilde{\boldsymbol{\rho}}_{\text{coa}} - \mathbf{R}_1^{-1} \mathbf{R}_3 \mathbf{K}_{\text{coa}}^{\circ} \mathbf{R}_1 \tilde{\boldsymbol{\rho}}_{\text{coa}}, \quad (51)$$

$$\tilde{\boldsymbol{\rho}}_{2\text{coa}} = \mathbf{K}_{\text{coa}}^{\circ} \mathbf{R}_1 \tilde{\boldsymbol{\rho}}_{\text{coa}}. \quad (52)$$

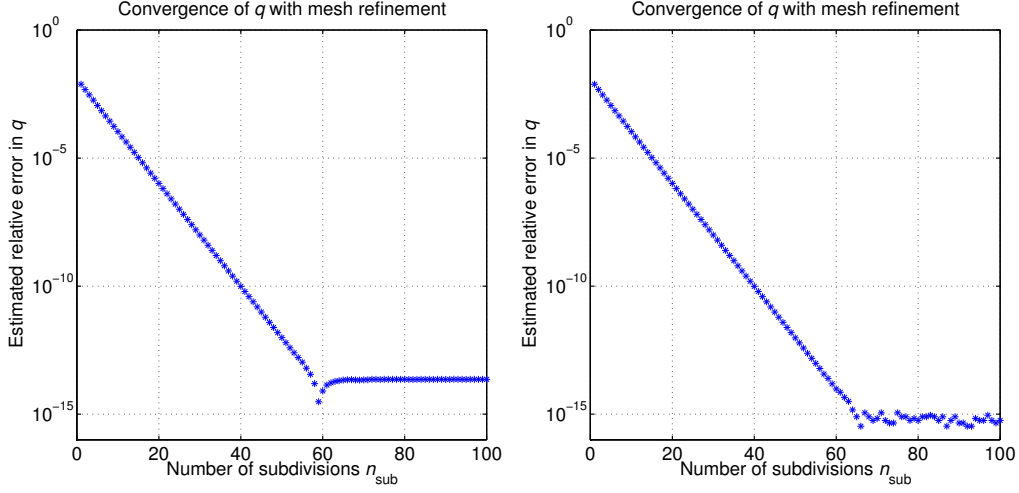


Figure 13: Convergence for  $q$  of (7) with  $\rho = \rho_1$  from (46). The curve  $\Gamma$  is as in (1) and  $\text{theta}=\pi/2$ ,  $\text{npan}=11$ , and  $\text{evec}=1$ . The reference values is taken as  $q = 1.95243329423584$ . Left: Results from the inner product preserving scheme of Appendix E produced with `demo10.m`. Right: Results with RCIP according to (53,54) produced with `demo10b.m`

The change of variables (51,52) is chosen so that the second block-row of (50) is automatically satisfied. The first block-row of (50) becomes

$$\begin{aligned} [\mathbf{I}_{\text{coa}} + \mathbf{M}_{\text{coa}}^{\circ} (\mathbf{R}_4 - \mathbf{R}_2 \mathbf{R}_1^{-1} \mathbf{R}_3) \mathbf{K}_{\text{coa}}^{\circ} \mathbf{R}_1 + \mathbf{M}_{\text{coa}}^{\circ} \mathbf{R}_2 \\ - \mathbf{R}_1^{-1} \mathbf{R}_3 \mathbf{K}_{\text{coa}}^{\circ} \mathbf{R}_1] \tilde{\rho}_{\text{coa}} = \mathbf{g}_{\text{coa}}. \end{aligned} \quad (53)$$

When (53) has been solved for  $\tilde{\rho}_{\text{coa}}$ , the weight-corrected version of the original density  $\rho_1$  can be recovered as

$$\hat{\rho}_{1\text{coa}} = \mathbf{R}_1 \tilde{\rho}_{\text{coa}}. \quad (54)$$

Figure 13 shows results for (46) with  $M$  being the double layer potential

$$M\rho(r) \equiv -2 \int_{\Gamma} \frac{\partial G}{\partial \nu'}(r, r') \rho(r') d\ell' = \frac{1}{\pi} \int_{\Gamma} \rho(\tau) \Im \left\{ \frac{d\tau}{\tau - z} \right\}. \quad (55)$$

The left image shows the convergence of  $q$  of (7) with  $n_{\text{sub}}$  using the inner product preserving discretization scheme of Appendix E for (46) as implemented in `demo10.m`. The right image shows  $q$  produced with RCIP according to (53,54) as implemented in `demo10b.m`. The reference value for  $q$  is computed with the program `demo10c.m`, which uses inner product preserving discretization together with compensated summation [37, 38] in order to enhance the achievable accuracy. One can see that, in addition to being

faster, RCIP gives an extra digit of accuracy. Actually, it seems as if the scheme in `demo10.m` converges to a  $q$  that is slightly wrong.

In conclusion, in this example and in terms of stability, the RCIP method is better than standard inner product preserving discretization and on par with inner product preserving discretization enhanced with compensated summation. In terms of computational economy and speed, RCIP greatly outperforms the two other schemes.

## 16 Nyström discretization of singular kernels

The Nyström scheme of Section 4 discretizes (6) using composite 16-point Gauss–Legendre quadrature. This works well when the kernel of the integral operator  $K$  is smooth on smooth  $\Gamma$ . When the kernel is not smooth on smooth  $\Gamma$ , then the quadrature fails and something better is needed. See [16] for a comparison of the performance of various modified high-order accurate Nyström discretizations for weakly singular kernels and [39] for a high-order general approach to the evaluation of layer potentials.

We are not sure what modified discretization is optimal in every situation. When nearly singular, weakly singular, and singular operators need to be discretized in the following, we chiefly use a modification to composite Gauss–Legendre quadrature called *local panelwise evaluation*. See [21, Section 2] and [25] for a description of this technique.

## 17 The exterior Dirichlet Helmholtz problem

Let  $D$  be the domain enclosed by the curve  $\Gamma$  and let  $E$  be the exterior to the closure of  $D$ . The exterior Dirichlet problem for the Helmholtz equation

$$\Delta U(r) + \omega^2 U(r) = 0, \quad r \in E, \quad (56)$$

$$\lim_{E \ni r \rightarrow r^\circ} U(r) = g(r^\circ), \quad r^\circ \in \Gamma, \quad (57)$$

$$\lim_{|r| \rightarrow \infty} \sqrt{|r|} \left( \frac{\partial}{\partial |r|} - i\omega \right) U(r) = 0, \quad (58)$$

has a unique solution  $U(r)$  under mild assumptions on  $\Gamma$  and  $g(r)$  [44] and can be modeled using a combined integral representation [11, Chapter 3]

$$U(r) = \int_{\Gamma} \frac{\partial \Phi_{\omega}}{\partial \nu'}(r, r') \rho(r') \, d\ell' - \frac{i\omega}{2} \int_{\Gamma} \Phi_{\omega}(r, r') \rho(r') \, d\ell', \quad r \in \mathbb{R}^2 \setminus \Gamma, \quad (59)$$

where  $\Phi_{\omega}(r, r')$  is the fundamental solution to the Helmholtz equation in two dimensions

$$\Phi_{\omega}(r, r') = \frac{i}{4} H_0^{(1)}(\omega |r - r'|). \quad (60)$$

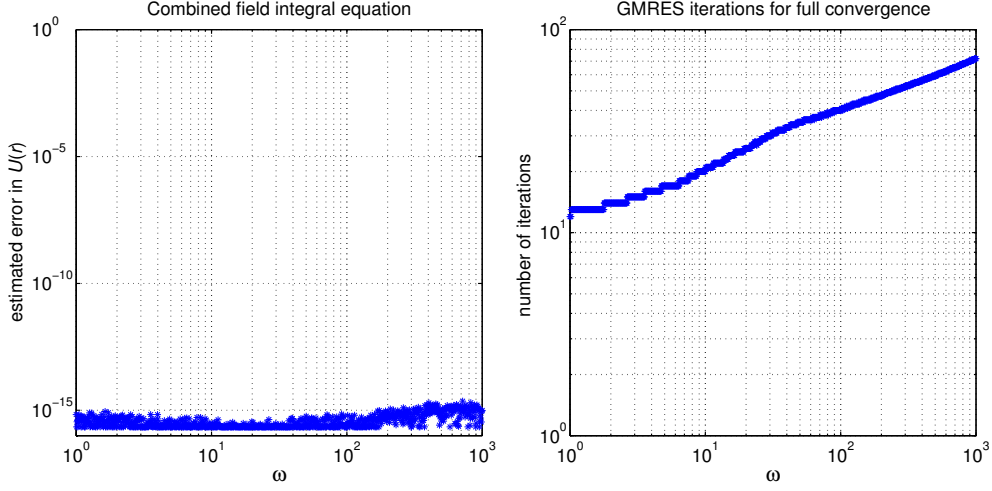


Figure 14: The exterior Dirichlet problem for Helmholtz equation with RCIP applied to (61). The program `demo11.m` is used with  $\Gamma$  as in (1) and  $\theta = \pi/2$ . The boundary condition  $g(r)$  of (57) is generated by a point source at  $(0.3, 0.1)$ . Left: the absolute error in  $U(r)$  at  $r = (-0.1, 0.2)$ . Right: the number of GMRES iterations needed to meet an estimated relative residual of  $\epsilon_{\text{mach}}$ .

Here  $H_0^{(1)}(\cdot)$  is the zeroth order Hankel function of the first kind. Insertion of (59) into (57) gives the combined field integral equation

$$\left( I + K_\omega - \frac{i\omega}{2} S_\omega \right) \rho(r) = 2g(r), \quad r \in \Gamma, \quad (61)$$

where

$$K_\omega \rho(r) = 2 \int_\Gamma \frac{\partial \Phi_\omega}{\partial \nu'}(r, r') \rho(r') d\ell', \quad (62)$$

$$S_\omega \rho(r) = 2 \int_\Gamma \Phi_\omega(r, r') \rho(r') d\ell'. \quad (63)$$

Figure 14 shows the performance of RCIP applied to (61) for 1000 different values of  $\omega \in [1, 10^3]$ . The program `demo11.m` is used. This program has a fixed-point initializer  $\mathbf{R}_*$ , see Section 11, whose construction only takes the leading asymptotic behavior of  $I + K_\omega - i\omega S_\omega/2$  at the corner vertex into account. The boundary  $\Gamma$  is as in (1) with  $\theta = \pi/2$  and the boundary conditions are chosen as  $g(r) = H_0^{(1)}(r - r')$  with  $r' = (0.3, 0.1)$  inside  $\Gamma$ . The error in  $U(r)$  of (59) is evaluated at  $r = (-0.1, 0.2)$  outside  $\Gamma$ . Since the magnitude of  $U(r)$  varies with  $\omega$ , peaking at about unity, the absolute error is shown rather than the relative error. The number of panels on the coarse mesh is chosen as `npan=0.6*omega+18` rounded to the nearest integer.

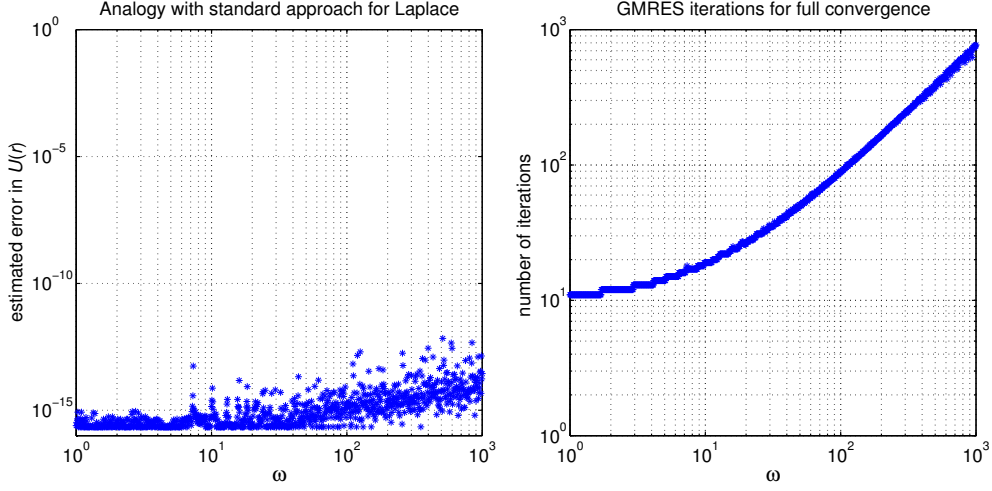


Figure 15: The exterior Neumann problem for Helmholtz equation with RCIP applied to (69). The program `demo12.m` is used with  $\Gamma$  as in (1) and  $\theta = \pi/2$ . The boundary condition  $g(r)$  of (65) is generated by a point source at  $(0.3, 0.1)$ . Left: the absolute error in  $U(r)$  at  $r = (-0.1, 0.2)$ . Right: the number of GMRES iterations needed to meet an estimated relative residual of  $\epsilon_{\text{mach}}$ .

## 18 The exterior Neumann Helmholtz problem

The exterior Neumann problem for the Helmholtz equation

$$\Delta U(r) + \omega^2 U(r) = 0, \quad r \in E, \quad (64)$$

$$\lim_{E \ni r \rightarrow r^\circ} \nu^\circ \cdot \nabla U(r) = g(r^\circ), \quad r^\circ \in \Gamma, \quad (65)$$

$$\lim_{|r| \rightarrow \infty} \sqrt{|r|} \left( \frac{\partial}{\partial |r|} - i\omega \right) U(r) = 0, \quad (66)$$

has a unique solution  $U(r)$  under mild assumptions on  $\Gamma$  and  $g(r)$  [44] and can be modeled as an integral equation in several ways. We shall consider two options: an “analogy with the standard approach for Laplace’s equation”, which is not necessarily uniquely solvable for all  $\omega$ , and a “regularized combined field integral equation” which is always uniquely solvable. See, further, [3, 9].

### 18.1 An analogy with the standard Laplace approach

Let  $K_\omega^A$  be the adjoint to the double-layer integral operator  $K_\omega$  of (62)

$$K_\omega^A \rho(r) = 2 \int_\Gamma \frac{\partial \Phi_\omega}{\partial \nu}(r, r') \rho(r') d\ell'. \quad (67)$$



Insertion of the integral representation

$$U(r) = \int_{\Gamma} \Phi_{\omega}(r, r') \rho(r') d\ell', \quad r \in \mathbb{R}^2 \setminus \Gamma \quad (68)$$

into (65) gives the integral equation

$$(I - K_{\omega}^A) \rho(r) = -2g(r), \quad r \in \Gamma. \quad (69)$$

Figure 15 shows the performance of RCIP applied to (69). The program `demo12.m` is used and the setup is the same as that for the Dirichlet problem in Section 17. A comparison between Figure 15 and Figure 14 shows that the number of GMRES iterations needed for full convergence now grows much faster with  $\omega$ . Furthermore, the relative error in the solution to the Neumann problem is larger, particularly so when  $\omega$  happens to be close to values for which the operator  $I - K_{\omega}^A$  in (69) has a nontrivial null space. Recall that (61) is always uniquely solvable while (69) is not.

## 18.2 A regularized combined field integral equation

The literature on regularized combined field integral equations for the exterior Neumann problem is rich and several formulations have been suggested. We shall use the representation [9]

$$U(r) = \int_{\Gamma} \Phi_{\omega}(r, r') \rho(r') d\ell' + i \int_{\Gamma} \frac{\partial \Phi_{\omega}}{\partial \nu'}(r, r') (S_{i\omega} \rho)(r') d\ell', \quad r \in \mathbb{R}^2 \setminus \Gamma, \quad (70)$$

which after insertion into (65) gives the integral equation

$$(I - K_{\omega}^A - iT_{\omega} S_{i\omega}) \rho(r) = -2g(r), \quad r \in \Gamma, \quad (71)$$

where

$$T_{\omega} \rho(r) = 2 \int_{\Gamma} \frac{\partial^2 \Phi_{\omega}}{\partial \nu \partial \nu'}(r, r') \rho(r') d\ell'. \quad (72)$$

The hypersingular operator  $T_{\omega}$  of (72) can be expressed as a sum of a simple operator and an operator that requires differentiation with respect to arc length only [41]

$$T_{\omega} \rho(r) = 2\omega^2 \int_{\Gamma} \Phi_{\omega}(r, r') (\nu \cdot \nu') \rho(r') d\ell' + 2 \int_{\Gamma} \frac{d\Phi_{\omega}}{d\ell}(r, r') \frac{d\rho}{d\ell'}(r') d\ell'. \quad (73)$$

This makes it possible to write (71) in the form

$$(I + A + B_1 B_2 + C_1 C_2) \rho(r) = -2g(r), \quad r \in \Gamma, \quad (74)$$

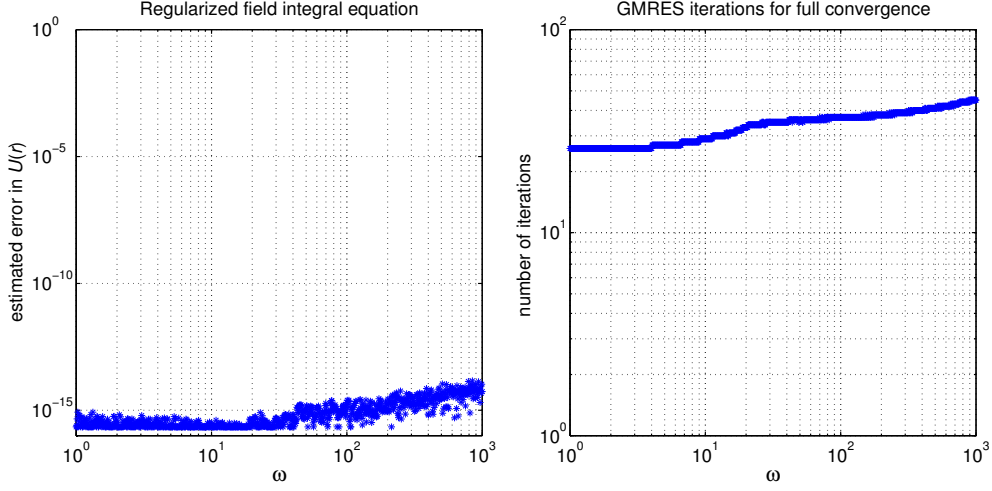


Figure 16: The same exterior Neumann problem for Helmholtz equation as in Figure 15, but RCIP is now applied to (74). The program `demo13b.m` is used.

where  $A = -K_\omega^A$ ,  $B_2 = S_{i\omega}$ , and the action of the operators  $B_1$ ,  $C_1$ , and  $C_2$  is given by

$$B_1\rho(r) = -2i\omega^2 \int_{\Gamma} \Phi_\omega(r, r')(\nu \cdot \nu')\rho(r') d\ell', \quad (75)$$

$$C_1\rho(r) = -2i \int_{\Gamma} \frac{d\Phi_\omega}{d\ell}(r, r')\rho(r') d\ell', \quad (76)$$

$$C_2\rho(r) = 2 \int_{\Gamma} \frac{d\Phi_{i\omega}}{d\ell}(r, r')\rho(r') d\ell'. \quad (77)$$

All integral operators in (74) are such that their discretizations admit the low-rank decomposition (17). We use the temporary expansion technique of Section 15 for (74), with two new layer densities that are later eliminated, to arrive at a single compressed equation analogous to (53). That equation involves nine equi-sized blocks of the compressed inverse  $\mathbf{R}$ .

Solving the problem in the example of Section 18.1 again, we now take the number of panels on the coarse mesh as `npan=0.6*omega+48` rounded to the nearest integer. Figure 16 shows results from the program `demo13b.m`. The resonances, visible in Figure 15, are now gone. It is interesting to observe in Figure 16 that, despite the presence of several singular operators and compositions in (74), the results produced with RCIP are essentially fully accurate and the number of GMRES iterations needed for convergence grows very slowly with  $\omega$ .

The program `demo13c.m` differs from `demo13b.m` in that it uses *local regularization* [21, Section 2.1] for the Cauchy-singular operators of (76) and (77) rather than local panelwise evaluation. The results produced by the two programs are virtually identical. We do not show yet another figure.

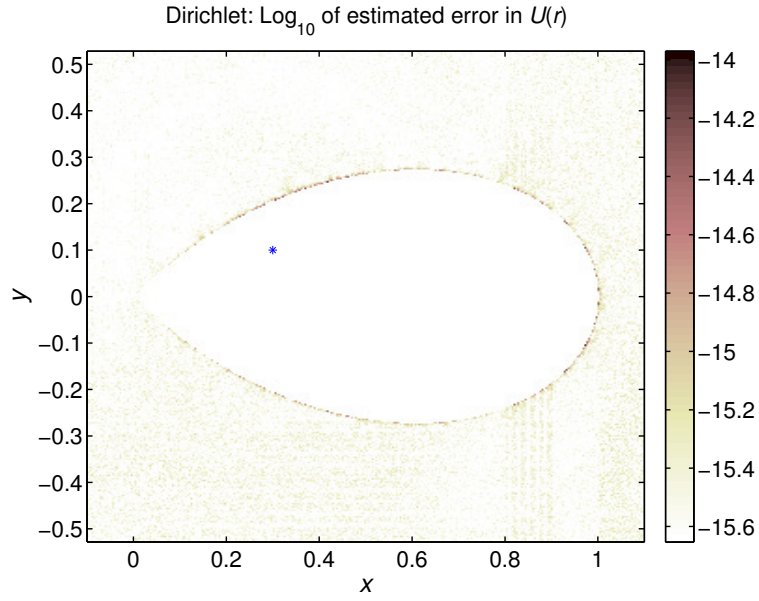


Figure 17: The error in the solution  $U(r)$  to the exterior Dirichlet Helmholtz problem. The coarse grid on  $\Gamma$  has 896 discretization points and  $U(r)$  is evaluated at 62392 points on a Cartesian grid in  $E$  using `demo11b.m` with  $\omega = 10$ . The source at  $r' = (0.3, 0.1)$  is shown as a blue star.

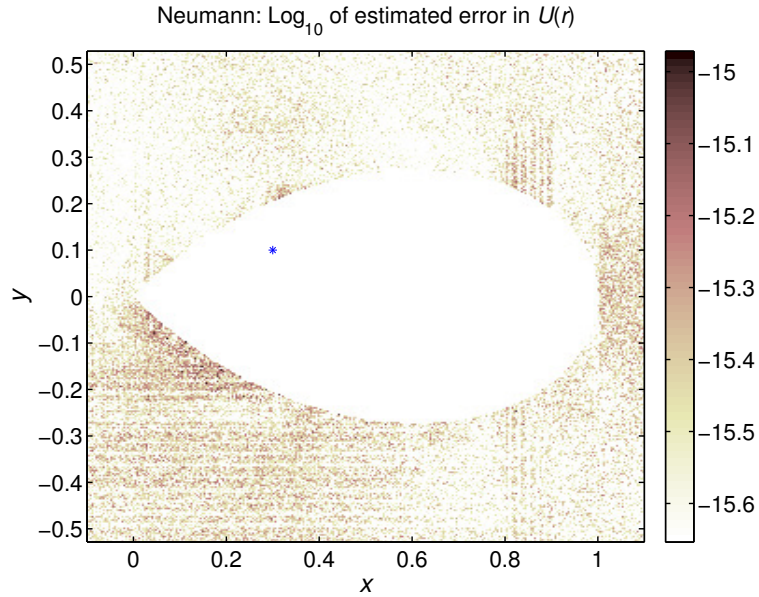


Figure 18: Same as Figure 17, but the exterior Neumann Helmholtz problem is solved using `demo13d.m`. The accuracy is even higher than in Figure 17.

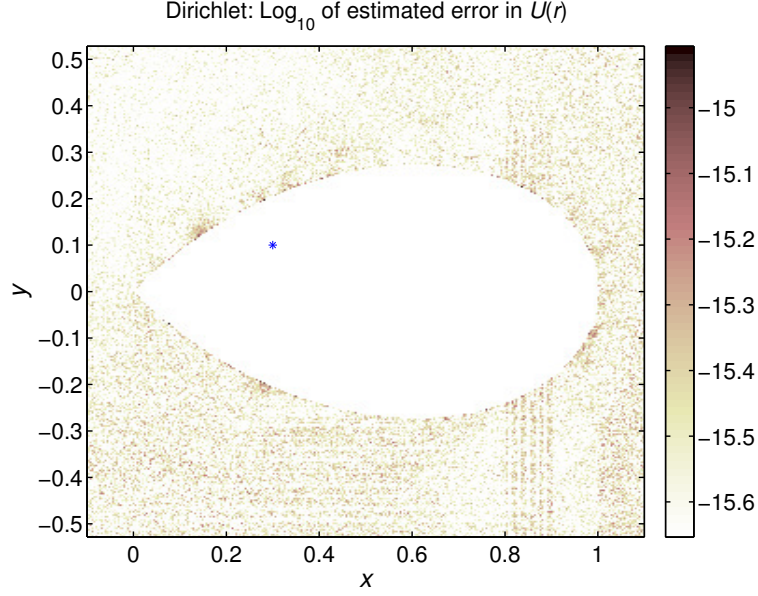


Figure 19: Same as Figure 17, but with `demo11e.m`. Local coordinates are used on  $\Gamma$  and the accuracy in  $U(r)$  is improved with up to one digit.

## 19 Field evaluations

Strictly speaking, a boundary value problem is not properly solved until its solution can be accurately evaluated in the *entire* computational domain. The program `demo11b.m` is a continuation of `demo11.m` which, after solving (61) for  $\tilde{\rho}_{\text{coa}}$  with RCIP and forming  $\hat{\rho}_{\text{coa}}$  via (26), computes the solution  $U(r)$  via (59) using three slightly different discretizations:

- (i) When  $r$  is away from  $\Gamma$ , 16-point Gauss–Legendre quadrature is used in (59) on all quadrature panels.
- (ii) When  $r$  is close to  $\Gamma$ , but not close to a panel neighboring a corner, 16-point Gauss–Legendre quadrature is used in (59) on panels away from  $r$  and local panelwise evaluation is used for panels close to  $r$ .
- (iii) When  $r$  is close to a panel neighboring a corner, the density  $\tilde{\rho}_{\text{coa}}$  is first used to reconstruct  $\hat{\rho}_{\text{part}}$  according to Section 9. Then 16-point Gauss–Legendre quadrature is used in (59) on panels away from  $r$  and local panelwise evaluation is used for panels close to  $r$ .

The first two discretizations only use the coarse grid on  $\Gamma$ . The third discretization needs a grid on a partially refined mesh on  $\Gamma$ .

The program `demo13d.m` is a continuation of `demo13b.m` which, after solving (71) with RCIP as described in Section 18.2, computes the solution  $U(r)$  via (70) using the three discretizations of the previous paragraph.

Figure 17 and Figure 18 show that RCIP in conjunction with the quadrature of [21, Section 2] can produce very accurate solutions to exterior Helmholtz problems in, essentially, the entire computational domain.

The main source of error in the computed field  $U(r)$  of Figure 17 is cancellation in the evaluation of the difference  $r - r'$  for  $r \in \Gamma$ . The program `demo11b.m` needs such differences in the discretized kernels of (62) and (63) and the vectors  $r$  and  $r'$  are individually evaluated in global coordinates via (1). The program `demo11e.m` is the same as `demo11b.m`, but with  $r - r'$  computed in local coordinates whenever  $r'$  is close to  $r \in \Gamma$ . A comparison of Figure 19 with Figure 17 shows that the use of local coordinates on  $\Gamma$  lead to an improved quality in  $\rho(r)$  which, in turn, affects  $U(r)$ . The improvement is most pronounced for  $U(r)$  close to  $\Gamma$ .

Further examples for the Helmholtz equation in non-smooth domains and more details on the discretization of Hankel kernels are found in [25, 27].

## 20 A Helmholtz transmission problem

A transmission problem for the Helmholtz equation can be formulated as

$$\Delta U(r) + \omega_1^2 U(r) = 0, \quad r \in E, \quad (78)$$

$$\Delta U(r) + \omega_2^2 U(r) = 0, \quad r \in D, \quad (79)$$

$$\lim_{E \ni r \rightarrow r^\circ} U(r) = \lim_{D \ni r \rightarrow r^\circ} U(r), \quad r^\circ \in \Gamma, \quad (80)$$

$$\lim_{E \ni r \rightarrow r^\circ} \frac{1}{\gamma_1} \nu^\circ \cdot \nabla U(r) = \lim_{D \ni r \rightarrow r^\circ} \frac{1}{\gamma_2} \nu^\circ \cdot \nabla U(r), \quad r^\circ \in \Gamma, \quad (81)$$

where  $\gamma_1$  and  $\gamma_2$  are material parameters associated with the exterior  $E$  and the interior  $D$ , respectively. We separate  $U(r)$  into an incoming field  $U^{\text{in}}(r)$  and a scattered field represented by two layer densities  $\rho$  and  $\mu$  so that for  $r \in E$

$$U(r) = U^{\text{in}}(r) + \gamma_1 \int_{\Gamma} \frac{\partial \Phi_{\omega_1}}{\partial \nu'}(r, r') \mu(r') d\ell' + \int_{\Gamma} \Phi_{\omega_1}(r, r') \rho(r') d\ell' \quad (82)$$

and for  $r \in D$

$$U(r) = \gamma_2 \int_{\Gamma} \frac{\partial \Phi_{\omega_2}}{\partial \nu'}(r, r') \mu(r') d\ell' + \int_{\Gamma} \Phi_{\omega_2}(r, r') \rho(r') d\ell'. \quad (83)$$

By this, the scattered field satisfies the outgoing radiation condition (58).

Insertion of (82) and (83) into (80) and (81) gives the system of integral equations [14, Eq. (11)] with compact (differences of) operators

$$\begin{bmatrix} I - \alpha_2 K_{\omega_2} + \alpha_1 K_{\omega_1} & -\alpha_4 (S_{\omega_2} - S_{\omega_1}) \\ \alpha_3 (T_{\omega_2} - T_{\omega_1}) & I + \alpha_1 K_{\omega_2}^A - \alpha_2 K_{\omega_1}^A \end{bmatrix} \begin{bmatrix} \mu(r) \\ \rho(r) \end{bmatrix} = \begin{bmatrix} g_1(r) \\ g_2(r) \end{bmatrix}, \quad (84)$$

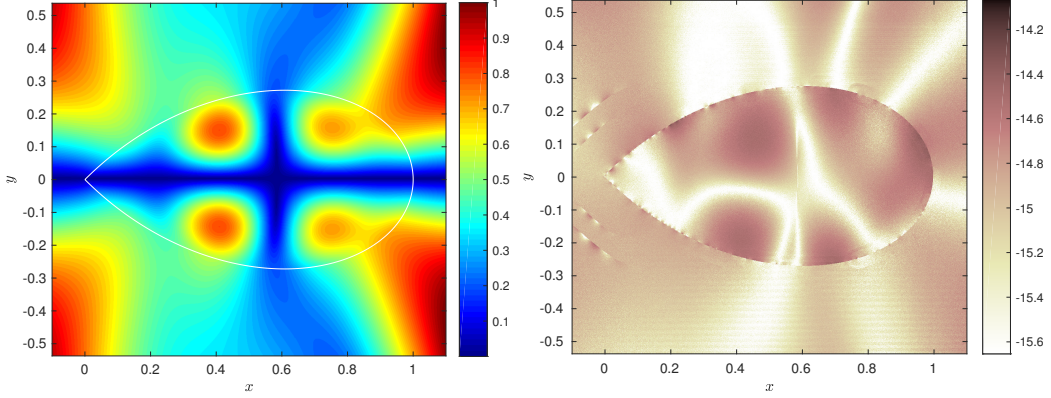


Figure 20: Left: magnitude of a normalized eigenfield,  $|U(r)|$ , at eigen-wavenumber  $\omega_1 = 9.701129417644246 - 2.000374579086419i$ . The coarse grid on  $\Gamma$  has 320 discretization points.  $U(r)$  is evaluated at  $10^6$  field points on a Cartesian grid in the computational domain. Right:  $\log_{10}$  of estimated absolute error in  $|U(r)|$ . The program `demo19.m` is used.

and with

$$g_1(r) = -2\alpha_4 U^{\text{in}}(r), \quad g_2(r) = 2\alpha_2 \frac{\partial U^{\text{in}}}{\partial \nu}(r), \quad (85)$$

$$\alpha_1 = \frac{\gamma_1}{\gamma_1 + \gamma_2}, \quad \alpha_2 = \frac{\gamma_2}{\gamma_1 + \gamma_2}, \quad \alpha_3 = \frac{\gamma_1 \gamma_2}{\gamma_1 + \gamma_2}, \quad \alpha_4 = \frac{1}{\gamma_1 + \gamma_2}. \quad (86)$$

We investigate the performance of RCIP applied to (84) for the purpose of finding resonant modes. The boundary  $\Gamma$  is as in (1) with  $\theta = \pi/2$ . We set  $\gamma_2 = 2.25$ ,  $\gamma_1 = 1$ ,  $\omega_2 = 1.5\omega_1$ ,  $U^{\text{in}}(r) = 0$  and look for  $\omega_1$ ,  $\rho$  and  $\mu$  that are non-trivial solutions to the homogeneous system (84). Unfortunately, the system (84) seems to admit false resonances, that is non-trivial solutions with  $\Im\{\omega_1\} < 0$  whose corresponding  $\rho$  and  $\mu$  generate eigenfields that are null-fields when inserted in (82) and (83). A true resonance is found at  $\omega_1 = 9.701129417644246 - 2.000374579086419i$ . The corresponding eigenfield  $U(r)$  is shown in Figure 20 along with a plot of the estimated field error. The coarse grid on  $\Gamma$  has 320 discretization points. The reference solution is computed with 50 per cent more points. The program `demo19.m` is used.

## 21 Close-to-touching objects

The usefulness of RCIP is not restricted to corner problems. RCIP works well also in more general contexts where solutions to integral equations exhibit some sort of (near) singularities. This section is about two such problems. First we compute the polarizability  $q$  of a pair of close-to-touching and highly conducting unit disks embedded in a background unit medium.

Then we proceed to doubly periodic boundary conditions and compute the effective conductivity  $\sigma_{\text{eff}}$  of a square array of conducting disks.

### 21.1 The two-disk problem

The setup is shown in Figure 21. This problem can be modeled with (3) and (7) and

$$\lambda = \frac{\sigma_2 - \sigma_1}{\sigma_2 + \sigma_1} . \quad (87)$$

To avoid stability problems for  $\lambda$  close to one, we instead use an alternative formulation which in complex notation reads [31, Eqs. (9,10)]

$$\mu(z) + \frac{\lambda}{\pi} \int_{\Gamma} \mu(\tau) \Im \left\{ \frac{d\tau}{\tau - z} \right\} = 2\lambda \Im \{ \bar{e} z \} , \quad z \in \Gamma , \quad (88)$$

$$q = -\sigma_1 \int_{\Gamma} \mu(z) \Re \{ \bar{e} dz \} . \quad (89)$$

RCIP can now be applied by considering  $r = (-d/2, 0)$  and  $r = (d/2, 0)$  to be singular boundary points treated in tandem. The subset  $\Gamma^*$  then covers the eight panels (four on each disk boundary) that are closest to the origin. Families of twelve-panel type **b** meshes are constructed in analogy with the procedure in Section 6.2. The superscript  $\star$  in  $\mathbf{K}_{ib}^{\star}$  indicates that only entries

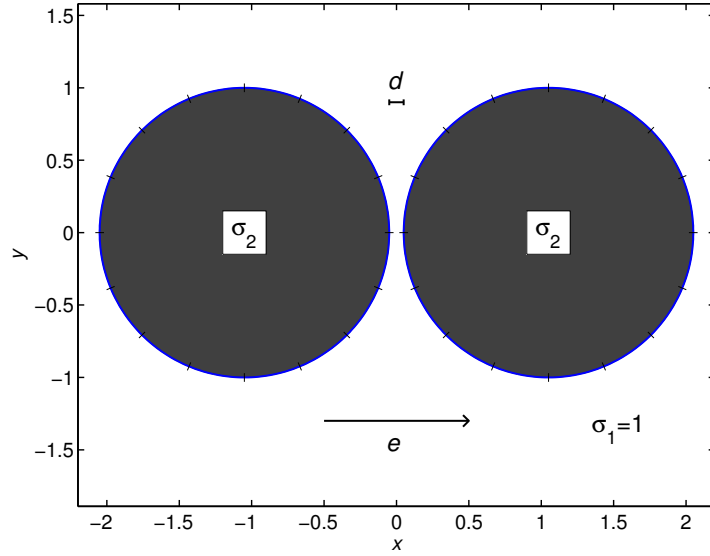


Figure 21: Two unit disks with conductivity  $\sigma_2 > 1$  are separated by a distance  $d$  and embedded in an infinite plane with conductivity  $\sigma_1 = 1$ . A unit field  $e$  is applied in the  $x$ -direction. Equi-sized quadrature panels are placed on the circles in such a way that there are breakpoints at  $r = (-d/2, 0)$  and  $r = (d/2, 0)$ .

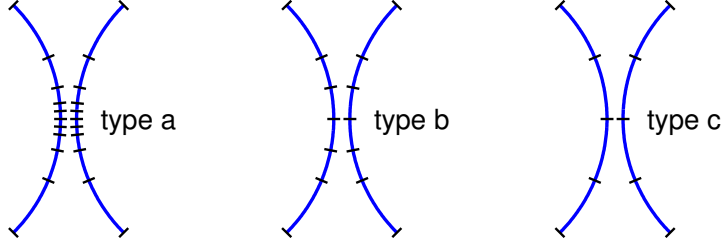


Figure 22: Meshes of type a, type b, and type c on the boundary subset  $\Gamma_i^*$  for the two-disk problem and for  $i = n_{\text{sub}} = 3$ . The type a mesh has  $8 + 4i$  panels. The type b mesh has twelve panels. The type c mesh has eight panels. The type a mesh is the restriction of the fine mesh to  $\Gamma_i^*$ . For  $i = n_{\text{sub}}$ , the type c mesh is the restriction of the coarse mesh to  $\Gamma^*$ . The type a mesh and the type b mesh coincide for  $i = 1$ .

with both indices corresponding to points on the eight innermost panels of a type b mesh are retained. The derivation of the recursion in Appendix D uses meshes of type a and type c with twice the number of panels compared to the single corner case. See Figure 22 and compare Figure 32.

The two-disk problem of Figure 21 is, in a sense, harder to solve than the one-corner model problem of Section 3. The reason being that the fine mesh on  $\Gamma$  for the two-disk problem has many panels that lie close to each other and where special quadratures techniques, see Section 16, need to be activated in the discretization of (88). This, in turn, slows down convergence and may even endanger the validity of the basic assumptions (17) and (D.3) upon which the entire RCIP scheme rests. The prolongation in (17) and (D.3) only holds on panels where standard quadrature is sufficient. In the one-corner model problem, on the other hand, special quadrature is barely needed. The basic assumptions (17) and (D.3) hold with, say, standard 16-point Gauss–Legendre quadrature provided that the opening angle  $\theta$  is not too small.

The families of meshes introduced in Figure 22 are constructed with the validity of (17) and (D.3) in mind. When constructing  $\mathbf{K}_{ib}^o$  in the recursion (22) and in (D.3), special quadrature may be activated in the discretization on meshes of type b if needed. Note, however, that the need for special quadrature will only arise for source points on the eight panels farthest away from the origin. For source points on the innermost four panels of type b meshes, standard quadrature is enough. The same is true for  $\mathbf{K}_{ia}^o$  in (D.3): special quadrature on meshes of type a needs only to be activated on the eight panels farthest away from the origin which are common to type a and type b meshes and where no prolongation takes place. Therefore (D.3) holds provided the order of the Gauss–Legendre quadrature is sufficiently high. Numerical experiments indicate that 22-point quadrature is sufficient.



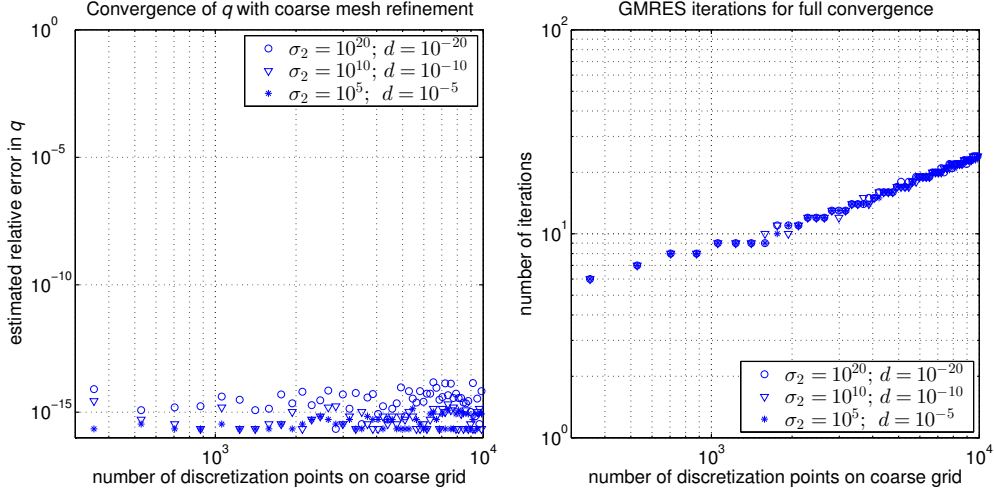


Figure 23: The two-disk problem of Figure 21 for the electrostatic equation and with RCIP applied to (88) and (89). The program `demo14.m` is used. Left: the estimated relative error in the polarizability  $q$  for various disks separation distances  $d$  and disk conductivities  $\sigma_2$ . Right: the number of GMRES iterations needed to meet an estimated relative residual of  $\epsilon_{\text{mach}}$ .

Figure 23 illustrates the performance of RCIP applied to (88) and (89) for the two-disk problem. The program `demo14.m` is used. Convergence is immediate and it appears as if rather extreme cases can be treated accurately. Reference values for  $q$  can be found in `demo14.m`.

**Remark:** The two-disk problem was addressed in [31, Section 10.3], but not solved with RCIP in its entirety due to the too simplistic mesh construction technique used in [31].

## 21.2 The square array of disks

The left image of Figure 24 shows the geometry of this classic problem. The following modification of (88) and (89) is used for modeling

$$\mu(z) + \frac{\lambda}{\pi} \int_{\Gamma_{\text{per}}} \mu(\tau) \Im \left\{ \frac{d\tau}{\tau - z} \right\} = 2\lambda \Im \{ \bar{e}z \}, \quad z \in \Gamma_{\text{unit}}, \quad (90)$$

$$\sigma_{\text{eff}} = \sigma_1 - \sigma_1 \int_{\Gamma_{\text{unit}}} \mu(z) \Re \{ \bar{e} dz \}, \quad (91)$$

where  $\Gamma_{\text{per}}$  refers to all disk interfaces in the plane,  $\Gamma_{\text{unit}}$  refers to the disk interface in the unit cell, see [19, Eqs. (13) and (14)], and  $\sigma_{\text{eff}}$  is the effective conductivity. The applied electric field is chosen as  $e = (1, 0)$ .

The disk separation distance  $d$  of Figure 24 may be expressed in terms

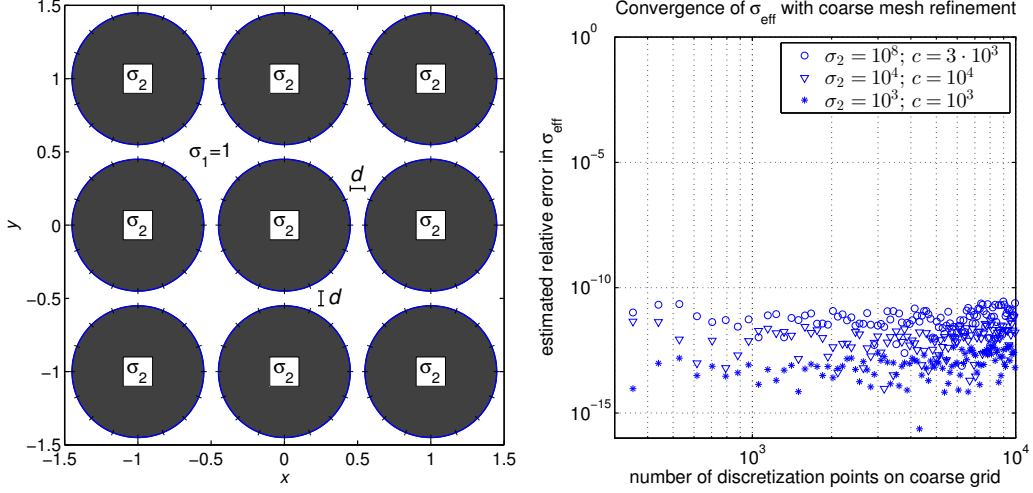


Figure 24: Left: a nine-unit-cell cutout from a square array of disks with conductivities  $\sigma_2$ . The background medium has  $\sigma_1 = 1$ . Right: the estimated relative error in  $\sigma_{\text{eff}}$  of (91) for three setups with different  $\sigma_2$  and separation distances  $d = 1/(c^2 + c\sqrt{c^2 - 1})$ . The program `demo14b.m` is used.

of a parameter  $c$  as

$$d = \frac{1}{c^2 + c\sqrt{c^2 - 1}}. \quad (92)$$

The higher the number  $\min\{c, \sigma_2/\sigma_1\}$ , the more difficult it is to compute  $\sigma_{\text{eff}}$  via traditional numerical methods [43].

We solve (90,91) for three setups:  $\sigma_2 = 10^8$  and  $c = 3 \cdot 10^3$ , which corresponds to the most extreme parameter choices in [10];  $\sigma_2 = 10^4$  and  $c = 10^4$ , which is the hardest test case of [17, Table 2]; and  $\sigma_2 = 10^3$  and  $c = 10^3$ , which is used both in [17, Table 2] and [18, Table 1]. The right image of Figure 24 shows that the RCIP-accelerated Nyström solver `demo14b.m` resolves  $\sigma_{\text{eff}}$  to full achievable accuracy already at 352 discretization points on the coarse grid on  $\Gamma_{\text{unit}}$  and that the results are stable under mesh refinement. The number of converged digits compares favorably to what is reported in [10, 17, 18]. Reference values and a uniformly valid asymptotic expression [43] for  $\sigma_{\text{eff}}$  are contained in `demo14b.m`.

## 22 Mixed boundary conditions

Elliptic PDEs with mixed boundary conditions, that is, Dirichlet conditions on parts of the boundary and Neumann conditions on the remaining contiguous parts (also known as Zaremba boundary conditions) can often be modeled using Fredholm second kind integral equations with operators that are smooth away from the points where the boundary conditions change

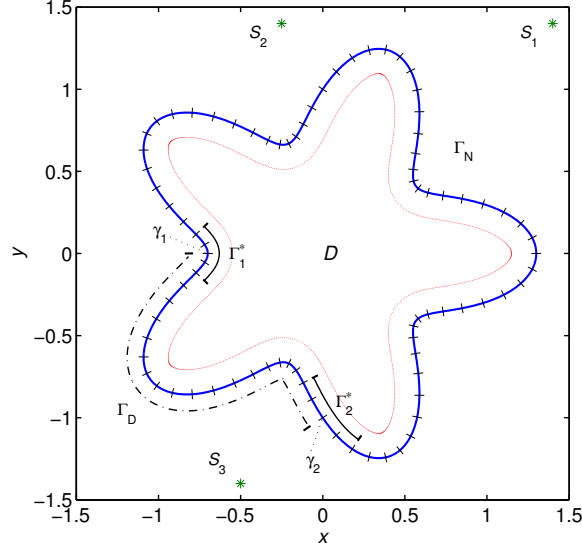


Figure 25: Interior domain  $D$  with boundary  $\Gamma = \Gamma_D \cup \Gamma_N$  given by (93) and (99). A coarse mesh is constructed on  $\Gamma$ . Two parts of the boundary,  $\Gamma_1^*$  and  $\Gamma_2^*$ , cover the four coarse panels closest to the singular boundary points  $\gamma_1$  and  $\gamma_2$  where the boundary conditions change type. The three sources  $S_k$  of (100), for the generation of boundary conditions, are marked by green stars. Thousand target points in  $D$  are marked by tiny red dots.

type. In this context, too, RCIP improves the stability and greatly reduces the computational cost of Nyström discretization schemes.

The paper [21] shows how to apply RCIP to mixed planar harmonic- and biharmonic problems. In this section we simply repeat two of the experiments in [21] for the purpose of disseminating the underlying MATLAB programs (`demo15.m` and `demo15b.m`).

The interior mixed problem for Laplace's equation is solved on the domain  $D$  bounded by the contour  $\Gamma$  with the parameterization

$$r(s) = (1 + 0.3 \cos(5s))(\cos(s), \sin(s)), \quad -\pi \leq s \leq \pi. \quad (93)$$

We seek a function  $U(r)$ , harmonic in  $D$ , such that

$$\lim_{D \ni r \rightarrow r^\circ} U(r) = g_D(r^\circ), \quad r^\circ \in \Gamma_D, \quad (94)$$

$$\lim_{D \ni r \rightarrow r^\circ} \nu^\circ \cdot \nabla U(r) = g_N(r^\circ), \quad r^\circ \in \Gamma_N, \quad (95)$$

where  $g_D(r)$  is Dirichlet data on the boundary part  $\Gamma_D$ ,  $g_N(r)$  is Neumann data on the boundary part  $\Gamma_N$ , and  $\Gamma_D \cup \Gamma_N = \Gamma$ . See Figure 25.

The solution  $U(r)$ ,  $r \in D \cup \Gamma_N$ , is represented by a density  $\rho(r)$ ,  $r \in \Gamma$ ,

$$U(z) = \frac{1}{\pi} \int_{\Gamma_D} \rho(\tau) \Im \left\{ \frac{d\tau}{\tau - z} \right\} - \frac{1}{\pi} \int_{\Gamma_N} \rho(\tau) \log |\tau - z| d|\tau|, \quad z \in D \cup \Gamma_N. \quad (96)$$

Insertion of (96) into (94) and (95) gives the system

$$\rho(z) + \frac{1}{\pi} \int_{\Gamma_D} \rho(\tau) \Im \left\{ \frac{d\tau}{\tau - z} \right\} - \frac{1}{\pi} \int_{\Gamma_N} \rho(\tau) \log |\tau - z| d|\tau| = g_D(z), \quad z \in \Gamma_D, \quad (97)$$

$$\rho(z) + \frac{1}{\pi} \int_{\Gamma_D} \rho(\tau) \Im \left\{ \frac{n_z d\tau}{(\tau - z)^2} \right\} + \frac{1}{\pi} \int_{\Gamma_N} \rho(\tau) \Re \left\{ \frac{n_z d|\tau|}{\tau - z} \right\} = g_N(z), \quad z \in \Gamma_N. \quad (98)$$

The boundary parts  $\Gamma_D$  and  $\Gamma_N$  are taken as

$$r(s) \in \Gamma_D, \quad -\pi < s < -\frac{\pi}{2}, \quad \text{and} \quad r(s) \in \Gamma_N, \quad -\frac{\pi}{2} < s < \pi, \quad (99)$$

and the boundary conditions  $g_D(r)$  and  $g_N(r)$  are constructed from a closed form reference solution

$$U_{\text{ref}}(z) = \Re \left\{ \sum_{k=1}^3 \frac{1}{z - S_k} \right\}, \quad (100)$$

where  $S_1 = 1.4 + 1.4i$ ,  $S_2 = -0.25 + 1.4i$ , and  $S_3 = -0.5 - 1.4i$  are sources outside of  $D$ , see Figure 25.

Figure 26 illustrates the performance of RCIP applied to (97) and (98). The program `demo15.m` is used. The solution  $U(r)$  is evaluated via (96) at the 1000 target points in  $D$  indicated by red dots in Figure 25. The rapid convergence and high achievable accuracy seen in Figure 26 means that RCIP resolves the mixed problem very well.

The program `demo15b.m` is about reconstruction. It is a simplified version of a program used in [21]. Once the solution  $\tilde{\rho}_{\text{coa}}$  is obtained, the discrete density  $\rho_{\text{fin}}$  is reconstructed on the fine grid on  $\Gamma$  using (33) and (34). The program `demo15b.m` also constructs  $U(r)$  on the fine grid on  $\Gamma_N$ , using [21, Eqs. (39), (40), and (49)], and then restricts  $U(r)$  to the coarse grid. Figure 27 shows results. The convergence and the achievable accuracy for  $U(r)$ ,  $r \in \Gamma_N$ , is similar to that of  $U(r)$  with  $r$  some distance away from  $\Gamma$ . Compare the right image of Figure 27 with the left image of Figure 26.

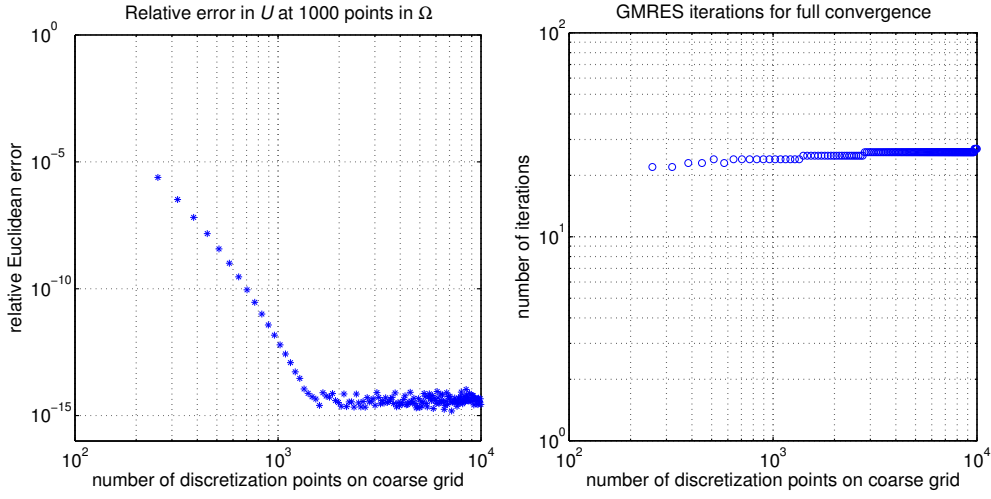


Figure 26: The mixed problem for Laplace's equation and with RCIP applied to (97) and (98). The program `demo15.m` is used. Left: convergence of  $U(r)$  at 1000 points  $r \in D$  with coarse mesh refinement. Right: the number of GMRES iterations needed to meet an estimated relative residual of  $\epsilon_{\text{mach}}$ .

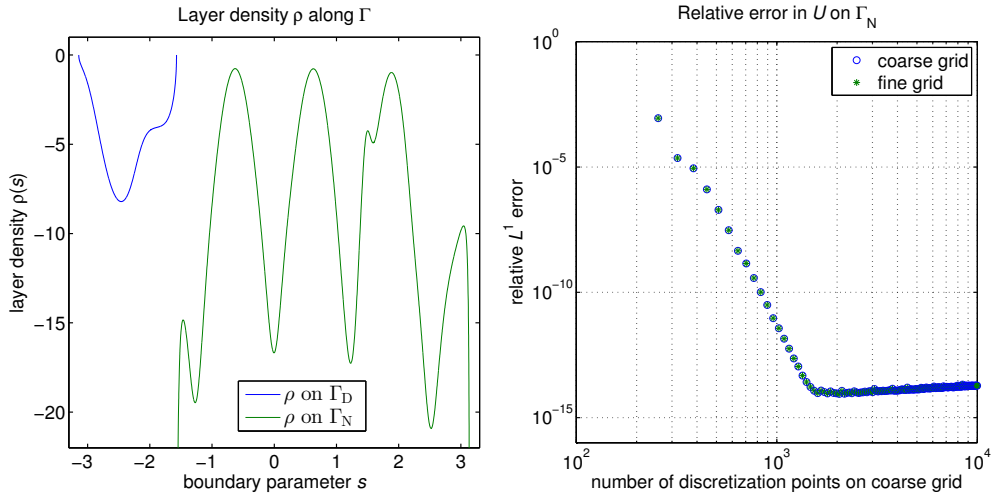


Figure 27: Same as in Figure 26 but `demo15b.m` is used. Left: reconstruction of the density  $\rho$  on the fine grid on  $\Gamma$ . Right: error in the reconstruction of the solution  $U(r)$ ,  $r \in \Gamma_N$ , on the coarse grid and on the fine grid.

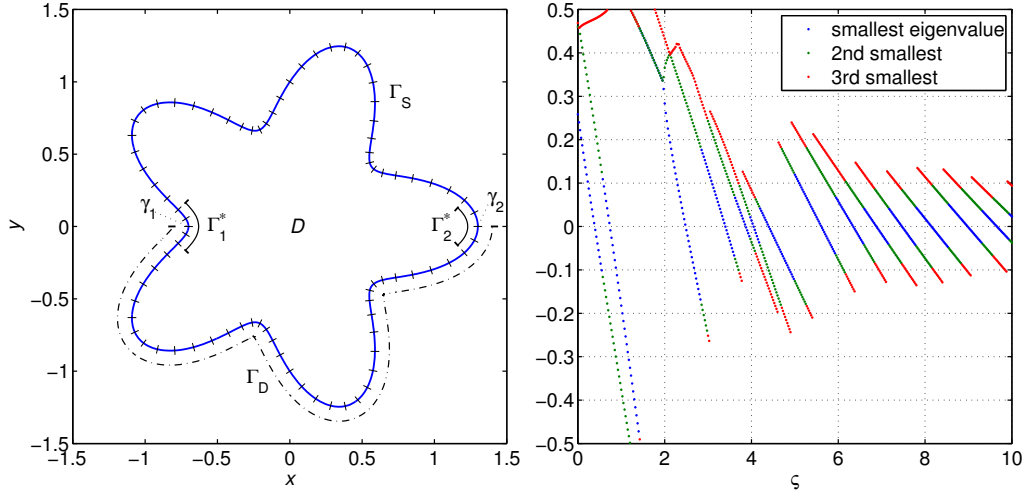


Figure 28: Left: similar to Figure 25, but with  $\Gamma = \Gamma_D \cup \Gamma_S$  according to (106). Right: Flow of the three system matrix eigenvalues of (107) with the smallest magnitude as a function of the Steklov parameter  $\zeta$ . The program `demo16c.m` is used. The Steklov eigenvalues are those values  $\zeta$  for which the smallest system matrix eigenvalue is zero.

## 23 Steklov eigenvalue problems

An interesting problem arises if the boundary conditions (94) and (95) of the interior mixed problem for Laplace's equation are changed into

$$\lim_{D \ni r \rightarrow r^\circ} U(r) = 0, \quad r^\circ \in \Gamma_D, \quad (101)$$

$$\lim_{D \ni r \rightarrow r^\circ} \nu^\circ \cdot \nabla U(r) = \zeta U(r^\circ), \quad r^\circ \in \Gamma_S. \quad (102)$$

Here the condition (102) on the boundary part  $\Gamma_S$  is called a Steklov boundary condition and  $\Gamma = \Gamma_D \cup \Gamma_S$ . Finding nontrivial harmonic solutions  $U(r)$  in  $D$  satisfying (101) and (102), along with associated values  $\zeta$ , is called a Steklov eigenvalue problem.

We solve the mixed Steklov eigenvalue problem on the smooth domain  $D$  given by (93) using the same representation for  $U(r)$  as in (96)

$$U(z) = \frac{1}{\pi} \int_{\Gamma_D} \rho(\tau) \Im \left\{ \frac{d\tau}{\tau - z} \right\} - \frac{1}{\pi} \int_{\Gamma_S} \rho(\tau) \log |\tau - z| d|\tau|, \quad z \in D \cup \Gamma_S. \quad (103)$$

Insertion of (103) into (101) and (102) gives the homogeneous system

$$\rho(z) + \frac{1}{\pi} \int_{\Gamma_D} \rho(\tau) \Im \left\{ \frac{d\tau}{\tau - z} \right\} - \frac{1}{\pi} \int_{\Gamma_S} \rho(\tau) \log |\tau - z| d|\tau| = 0, \quad z \in \Gamma_D, \quad (104)$$

$$\begin{aligned} \rho(z) + \frac{1}{\pi} \int_{\Gamma_D} \rho(\tau) \Im \left\{ \frac{n_z d\tau}{(\tau - z)^2} \right\} + \frac{1}{\pi} \int_{\Gamma_S} \rho(\tau) \Re \left\{ \frac{n_z d|\tau|}{\tau - z} \right\} \\ - \frac{\varsigma}{\pi} \int_{\Gamma_D} \rho(\tau) \Im \left\{ \frac{d\tau}{\tau - z} \right\} + \frac{\varsigma}{\pi} \int_{\Gamma_S} \rho(\tau) \log |\tau - z| d|\tau| = 0, \quad z \in \Gamma_S. \end{aligned} \quad (105)$$

The boundary parts  $\Gamma_D$  and  $\Gamma_S$  are taken from (93) as

$$r(s) \in \Gamma_D, \quad -\pi < s < 0, \quad \text{and} \quad r(s) \in \Gamma_S, \quad 0 < s < \pi, \quad (106)$$

see the left image of Figure 28.

Discretization of (104) and (105) together with RCIP leads to a linear system

$$(\mathbf{R}^{-1} + \mathbf{K}_{\text{coa1}}^\circ - \varsigma \mathbf{K}_{\text{coa2}}^\circ) \hat{\boldsymbol{\rho}}_{\text{coa}} = \mathbf{0}, \quad (107)$$

where  $\mathbf{R}$  depends on  $\varsigma$ , the matrix  $\mathbf{K}_{\text{coa1}}^\circ$  contains entries coming from the discretization of the integral operators in (104) and (105) that are not multiplied with  $\varsigma$ , and the entries of  $\mathbf{K}_{\text{coa2}}^\circ$  come from the discretization of the remaining operators. Values of  $\varsigma$  that correspond to a zero eigenvalue of the system matrix in (107) are solutions to the Steklov eigenvalue problem.

The right image of Figure 28, produced by the program `demo16c.m`, shows the three smallest system matrix eigenvalues of (107) as a function of  $\varsigma$ . The program `demo16d.m` uses an eigenvalue search algorithm [28, Section 9.1] to generate a table of the first 50 Steklov eigenvalues. The estimated relative accuracy is about  $10^{-14}$ .

### 23.1 Pure Steklov eigenvalue problem on a square

Setups where  $\Gamma = \Gamma_S$ , that is  $\Gamma_D = \emptyset$ , and where  $\Gamma$  is only piecewise smooth are of particular interest in spectral theory. Recently some fascinating open problems have emerged [13]. The program `demo16b.m` computes the 20 first pure Steklov eigenvalues on the square  $D = (-1, 1) \times (-1, 1)$  using a RCIP-accelerated solver very similar to that of `demo16d`. The numerical results are compared with results from the semi-analytic expressions of [13, Section 3.1]. The estimated relative accuracy is on the order of  $\epsilon_{\text{mach}}$ .

## 24 Limit polarizability

Let us return to (6) and write it in the form

$$(K - w) \rho(r) = g(r), \quad r \in \Gamma, \quad (108)$$

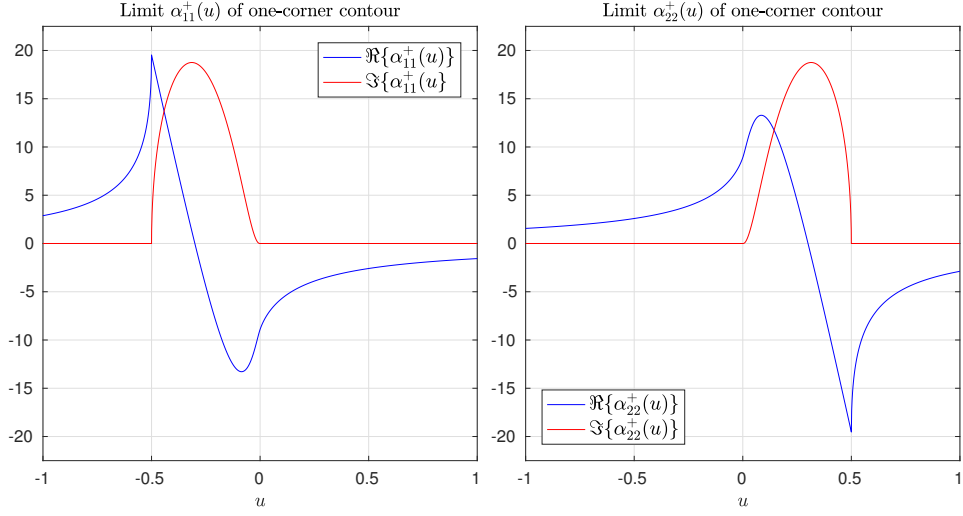


Figure 29: Elements  $\alpha_{11}^+(u)$  and  $\alpha_{22}^+(u)$  of the limit polarizability tensor for the object enclosed by  $\Gamma$  of (1) and with  $\theta = \pi/2$ . The program `demo17.m` is used.

where

$$w \equiv u + iv = -1/\lambda \quad (109)$$

is a new complex variable. Values of  $w$  for which (108) has no solution are points in the spectrum of  $K$ . The precise nature of this spectrum depends both on  $\Gamma$  and on the function space considered [33, 34]. On the “energy space”  $H^{-1/2}(\Gamma)$ , the spectrum of  $K$  is real and may have both discrete and continuous parts.

We solve (108) and compute the normalized polarizability

$$\alpha(w) = \frac{1}{|V|} \int_{\Gamma} \rho(r)(e \cdot r) \, d\ell, \quad (110)$$

where  $|V|$  is the area enclosed by  $\Gamma$ . We are particularly interested in  $\alpha^+(u)$ , that is, the limit of  $\alpha(w)$  as  $v \rightarrow 0^+$ . The programs used are extensions of `demo8b.m`: the construction of the initializer  $\mathbf{R}_*$  is accelerated using Newton’s method, as described in Section 12, and a homotopy method is used for the limit  $v \rightarrow 0^+$ , see [24, Section 6.3].

The program `demo17.m` computes  $\alpha^+(u)$  for  $\Gamma$  as in (1) and with  $\theta = \pi/2$ . The applied electric field is either  $e = (1, 0)$ , giving the element  $\alpha_{11}^+(u)$  of the limit polarizability tensor, or  $e = (0, 1)$ , giving  $\alpha_{22}^+(u)$ . Figure 29 shows results. By varying  $\theta$  in `demo17.m`, one can see that a continuous non-zero  $\Im\{\alpha^+(u)\}$  is only possible in the interval  $-|1 - \theta/\pi| < u < |1 - \theta/\pi|$ .

The program `demo17b.m` computes  $\alpha^+(u)$  for  $\Gamma$  being the unit square, compare [33, Figure 5(a)] where a similar MATLAB program is used. In addition, `demo17b.m` also computes the singularity exponent  $\beta$  in the leading



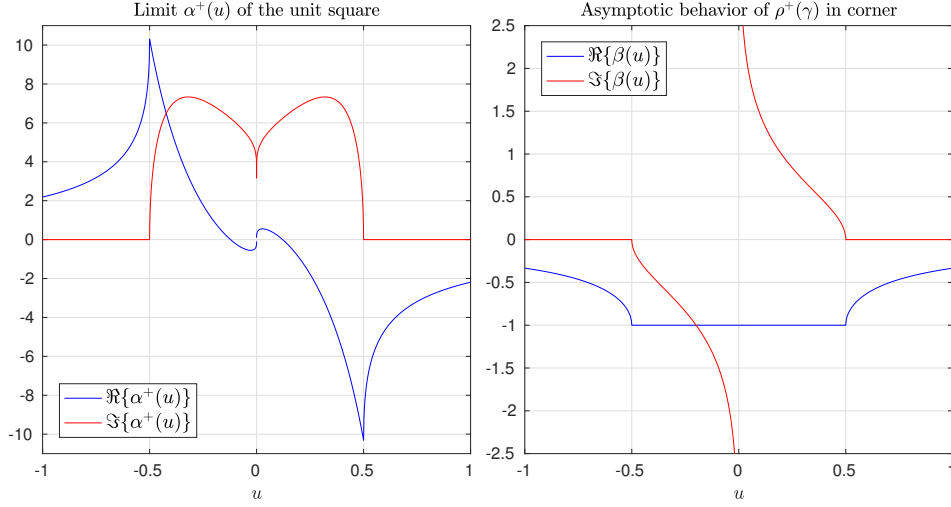


Figure 30: Left: the limit polarizability  $\alpha^+(u)$  of the unit square. Right: the leading exponent  $\beta(u)$  of (111) for the asymptotics of  $\rho^+(r)$  close to a corner vertex. The program `demo17b.m` is used.

asymptotic behavior of  $\rho^+(r)$  in the square corners,

$$\rho^+(\gamma) \propto \gamma^\beta, \quad (111)$$

where  $\gamma$  is the arc length distance to the nearest corner vertex, see Section 13. Figure 30 shows results. We emphasize that for  $v = 0$  and  $-0.5 < u < 0.5$ , there is no solution  $\rho(r)$  to (108). There is, however, a solution  $\rho(r) \in H^{-1/2}(\Gamma)$  for  $v$  arbitrarily close to 0 and it is the polarizability  $\alpha(w)$  corresponding to this limit solution, with  $v \rightarrow 0^+$ , that is depicted in the left image of Figure 30. Furthermore, the general polarizability  $\alpha(w)$  is simply related to the limit polarizability  $\Im\{\alpha^+(u)\}$  via

$$\alpha(w) = \frac{1}{\pi} \int_{-1}^1 \frac{\Im\{\alpha^+(s)\} ds}{s - w}, \quad (112)$$

see [33, Section 3]. One can say that  $\Im\{\alpha^+(u)\}/\pi$  is the derivative of a spectral measure associated with  $\alpha(w)$ .

## 25 Some computations on the cube

The applicability of RCIP acceleration to Nyström discretization of Fredholm second kind integral equations is not restricted to planar problems. It extends also to 3D. Rotationally symmetric surfaces that are smooth aside from isolated sharp edges or conical points are particularly simple to deal with [28, 34]. Surfaces that contain a mix of contiguous edges and corners

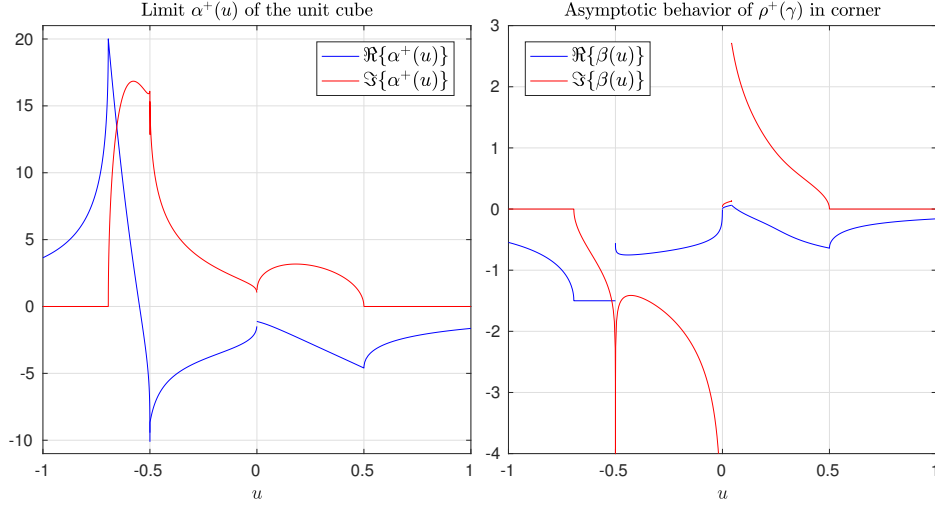


Figure 31: Left: the limit polarizability  $\alpha^+(u)$  of the unit cube.  $\Im\{\alpha^+(u)\}$  has support for  $u \in [-0.694525, 0.5]$ . Right: the leading exponent  $\beta(u)$  of (111) in the direction toward a cube corner vertex. The program `demo18.m` is used.

require that RCIP is applied in a two-step manner: First it is used to find multiplicative weight corrections that capture the singular behavior of  $\rho(r)$  in directions perpendicular to the edges using the techniques of Section 8. With these corrections incorporated into the standard quadrature,  $\rho(r)$  can be resolved on the coarse grid except for in the corners. There intense refinement has to take place and RCIP is used a second time.

Reference [33] details the two-step procedure for the solution of (108) on the surface of the unit cube. The action of the integral operator  $K$  in 3D is

$$K\rho(r) = - \int_{\Gamma} \frac{\nu \cdot (r - r') \rho(r') d\ell'}{2\pi|r - r'|^3}. \quad (113)$$

The left image of Figure 31, taken from [33], shows the limit polarizability  $\alpha^+(u)$  of the cube computed in this way.

The right image of Figure 31, produced by the program `demo18.m`, shows the vertex singularity exponent  $\beta(u)$  of a cube corner. The function  $\beta(u)$  is interesting since for some of its arguments there exist a number of benchmarks. For example, the quantity  $1 + \beta(-1)$  is a so-called “Fichera-type eigenvalue” for which the values 0.45417371 [49] and 0.454173734 [42] have been reported. Our estimate, produced by an upgraded version of `demo18.m`, is 0.45417373430(14). The two digits within parenthesis are extrapolated.

## Acknowledgements

The idea to make this tutorial came up during a discussion with Alex Barnett and Adrianna Gillman of 5/20/12 at the FACM’12 conference at NJIT. Input

and feedback from Alex and Adrianna, and from Shidong Jiang, Mary-Catherine Kropinski, Mikyoung Lim, David McKirdy, Rikard Ojala, and Karl-Mikael Perfekt has been of great value. The work was supported by the Swedish Research Council under contracts 621-2011-5516 and 621-2014-5159.

## \*\*\* Appendices \*\*\*

### Appendix A. Proof that $\mathbf{P}_W^T \mathbf{P} = \mathbf{I}_{\text{coa}}$

Let  $\mathbf{f}_{\text{coa}}$  and  $\mathbf{g}_{\text{coa}}$  be two column vectors, corresponding to the discretization of two panelwise polynomials with panelwise degree 15 on the coarse mesh of  $\Gamma$ . Then

$$\mathbf{f}_{\text{coa}}^T \mathbf{W}_{\text{coa}} \mathbf{g}_{\text{coa}} = (\mathbf{P} \mathbf{f}_{\text{coa}})^T \mathbf{W}_{\text{fin}} (\mathbf{P} \mathbf{g}_{\text{coa}}) = \mathbf{f}_{\text{coa}}^T \mathbf{P}^T \mathbf{W}_{\text{fin}} \mathbf{P} \mathbf{g}_{\text{coa}}, \quad (\text{A.1})$$

because composite 16-point Gauss–Legendre quadrature has panelwise polynomial degree 31. The diagonal matrix  $\mathbf{W}_{\text{coa}}$  has size  $16n_{\text{pan}} \times 16n_{\text{pan}}$ .

Since there are  $16n_{\text{pan}}$  linearly independent choices of  $\mathbf{f}_{\text{coa}}$  and of  $\mathbf{g}_{\text{coa}}$  it follows from (A.1) that

$$\mathbf{W}_{\text{coa}} = \mathbf{P}^T \mathbf{W}_{\text{fin}} \mathbf{P}, \quad (\text{A.2})$$

which, using (14), can be rewritten

$$\mathbf{I}_{\text{coa}} = \mathbf{W}_{\text{coa}}^{-1} \mathbf{P}^T \mathbf{W}_{\text{fin}} \mathbf{P} = \mathbf{P}_W^T \mathbf{P}. \quad (\text{A.3})$$

## Appendix B. Derivation of the compressed equation

The compression of (9), leading up to (18), was originally described in [31, Section 6.4]. Here we give a summary.

The starting point is (6) which, using the operator split analogous to (12,13)

$$K = K^\star + K^\circ \quad (\text{B.1})$$

and the variable substitution

$$\rho(z) = (I + \lambda K^\star)^{-1} \tilde{\rho}(z), \quad (\text{B.2})$$

gives the right preconditioned equation

$$\tilde{\rho}(z) + \lambda K^\circ (I + \lambda K^\star)^{-1} \tilde{\rho}(z) = \lambda g(z), \quad z \in \Gamma. \quad (\text{B.3})$$

Now, let us take a close look at (B.3). We observe that  $K^\circ (I + \lambda K^\star)^{-1}$  is an operator whose action on any function gives a function that is smooth on the innermost two panels of the coarse grid on  $\Gamma^\star$ . This is so since  $K^\circ$  is constructed so that its action on any function gives a function that is smooth on the innermost two panels of the coarse grid on  $\Gamma^\star$ . Furthermore, the right hand side  $\lambda g(z)$  of (B.3) is assumed to be panelwise smooth. Using an argument of contradiction we see that  $\tilde{\rho}(z)$  has to be a panelwise smooth function on the innermost two panels of the coarse grid on  $\Gamma^\star$ .

Having concluded that  $\tilde{\rho}(z)$  is panelwise smooth close to the corner we can write

$$\tilde{\rho}_{\text{fin}} = \mathbf{P} \tilde{\rho}_{\text{coa}}. \quad (\text{B.4})$$

We also have

$$\mathbf{g}_{\text{fin}} = \mathbf{P} \mathbf{g}_{\text{coa}}, \quad (\text{B.5})$$

the discrete version of (B.2) on the fine grid

$$\rho_{\text{fin}} = (\mathbf{I}_{\text{fin}} + \lambda \mathbf{K}_{\text{fin}}^\star)^{-1} \tilde{\rho}_{\text{fin}}, \quad (\text{B.6})$$

and the relations (13) and (17) which we now repeat:

$$\mathbf{K}_{\text{fin}} = \mathbf{K}_{\text{fin}}^\star + \mathbf{K}_{\text{fin}}^\circ, \quad (\text{B.7})$$

$$\mathbf{K}_{\text{fin}}^\circ = \mathbf{P} \mathbf{K}_{\text{coa}}^\circ \mathbf{P}_W^T. \quad (\text{B.8})$$

Substitution of (B.4,B.5,B.6,B.7,B.8) into (9), which we now repeat:

$$(\mathbf{I}_{\text{fin}} + \lambda \mathbf{K}_{\text{fin}}) \rho_{\text{fin}} = \lambda \mathbf{g}_{\text{fin}}, \quad (\text{B.9})$$

gives

$$\mathbf{P} \tilde{\rho}_{\text{coa}} + \lambda \mathbf{P} \mathbf{K}_{\text{coa}}^\circ \mathbf{P}_W^T (\mathbf{I}_{\text{fin}} + \lambda \mathbf{K}_{\text{fin}}^\star)^{-1} \mathbf{P} \tilde{\rho}_{\text{coa}} = \mathbf{P} \mathbf{g}_{\text{coa}}. \quad (\text{B.10})$$

Applying  $\mathbf{P}_W^T$  (or  $\mathbf{Q}$ ) to the left in (B.10) and using the identities (15) (or (31)) gives the compressed equation (18).

## Appendix C. Integration of $\rho$ against smooth $f$

This appendix is about computing integrals

$$\int_{\Gamma} f(r) \rho(r) \, d\ell, \quad (\text{C.1})$$

where  $\rho(r)$  is the solution to (6). It is assumed that  $f(r(s))|\dot{r}(s)|$  is a piecewise smooth function of the boundary parameter  $s$ . The aim is to derive the relation

$$\int_{\Gamma} f(r) \rho(r) \, d\ell = \sum_i \zeta_{\text{coa}_i} \hat{\rho}_{\text{coa}_i} w_{\text{coa}_i}, \quad (\text{C.2})$$

where

$$\zeta_i = f(r(s_i))|\dot{r}(s_i)| \quad (\text{C.3})$$

and the discrete weight-corrected density vector  $\hat{\rho}_{\text{coa}}$  is defined in (26).

The derivation uses (14,19,26,B.4,B.6) and the diagonal matrices  $\mathbf{W}_{\text{coa}}$  and  $\mathbf{W}_{\text{fin}}$  defined in Section 5 and goes as follows:

$$\begin{aligned} \int_{\Gamma} f(r) \rho(r) \, d\ell &= \int_0^1 f(r(s)) \rho(r(s)) |\dot{r}(s)| \, ds \\ &= \sum_i \zeta_{\text{fin}_i} \rho_{\text{fin}_i} w_{\text{fin}_i} \\ &= \zeta_{\text{fin}}^T \mathbf{W}_{\text{fin}} \boldsymbol{\rho}_{\text{fin}} \\ &= \zeta_{\text{fin}}^T \mathbf{W}_{\text{fin}} (\mathbf{I}_{\text{fin}} + \lambda \mathbf{K}_{\text{fin}}^*)^{-1} \tilde{\boldsymbol{\rho}}_{\text{fin}} \\ &= \zeta_{\text{coa}}^T \mathbf{P}^T \mathbf{W}_{\text{fin}} (\mathbf{I}_{\text{fin}} + \lambda \mathbf{K}_{\text{fin}}^*)^{-1} \mathbf{P} \tilde{\boldsymbol{\rho}}_{\text{coa}} \\ &= \zeta_{\text{coa}}^T \mathbf{W}_{\text{coa}} \mathbf{W}_{\text{coa}}^{-1} \mathbf{P}^T \mathbf{W}_{\text{fin}} (\mathbf{I}_{\text{fin}} + \lambda \mathbf{K}_{\text{fin}}^*)^{-1} \mathbf{P} \tilde{\boldsymbol{\rho}}_{\text{coa}} \\ &= \zeta_{\text{coa}}^T \mathbf{W}_{\text{coa}} \mathbf{P}_W^T (\mathbf{I}_{\text{fin}} + \lambda \mathbf{K}_{\text{fin}}^*)^{-1} \mathbf{P} \tilde{\boldsymbol{\rho}}_{\text{coa}} \\ &= \zeta_{\text{coa}}^T \mathbf{W}_{\text{coa}} \mathbf{R} \tilde{\boldsymbol{\rho}}_{\text{coa}} \\ &= \zeta_{\text{coa}}^T \mathbf{W}_{\text{coa}} \hat{\boldsymbol{\rho}}_{\text{coa}} \\ &= \sum_i \zeta_{\text{coa}_i} \hat{\rho}_{\text{coa}_i} w_{\text{coa}_i}. \end{aligned} \quad (\text{C.4})$$

## Appendix D. Derivation of the recursion

The recursion (22) for the rapid construction of the diagonal blocks of the compressed weighted inverse  $\mathbf{R}$  was originally derived in [31, Section 7] using different notation and different meshes than in the present tutorial. The recursion was derived a second time in [32, Section 7] using new meshes. Better notation was introduced in [21, Section 6]. A third derivation, in a general setting, takes place in [22, Section 5] and it uses the same notation and meshes as in the present tutorial.

A problem when explaining the derivation of (22) is that one needs to introduce intermediate meshes and matrices whose appearance may cause enervation at a first glance. Particularly so since these meshes and matrices are not needed in the final expression (22). We emphasize that the underlying matrix property that permits the recursion is the low rank of certain off-diagonal blocks in discretizations of  $K^\circ$  of (B.1) on nested meshes.

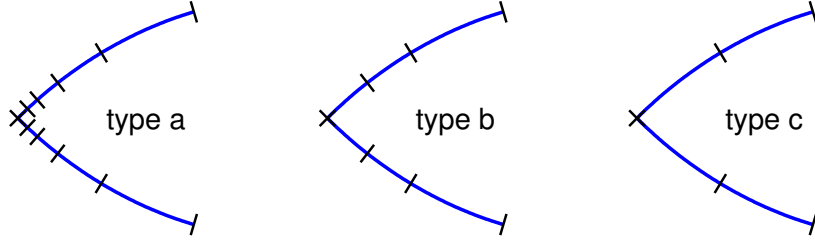


Figure 32: Meshes of type a, type b, and type c on the boundary subset  $\Gamma_i^*$  for  $i = n_{\text{sub}} = 3$ . The type a mesh has  $4 + 2i$  panels. The type b mesh has six panels. The type c mesh has four panels. The type a mesh is the restriction of the fine mesh to  $\Gamma_i^*$ . For  $i = n_{\text{sub}}$ , the type c mesh is the restriction of the coarse mesh to  $\Gamma^*$ . The type a mesh and the type b mesh coincide for  $i = 1$ .

The recursion (22) only uses one type of mesh explicitly – the type b mesh of Figure 5. On each  $\Gamma_i^*$  there is a type b mesh and a corresponding discretization of  $K^\circ$  denoted  $\mathbf{K}_{ib}^\circ$ . Here we need two new types of meshes denoted type a and type c, along with corresponding discrete operators. For example,  $\mathbf{K}_{ia}$  is the discretization of  $K$  on a type a mesh on  $\Gamma_i^*$ . The three types of meshes are depicted in Figure 32. Actually, a straight type c mesh was already introduced in Figure 4.

Now we define  $\mathbf{R}_i$  as

$$\mathbf{R}_i \equiv \mathbf{P}_{Wiac}^T (\mathbf{I}_{ia} + \lambda \mathbf{K}_{ia})^{-1} \mathbf{P}_{iac}, \quad (\text{D.1})$$

where  $\mathbf{P}_{Wiac}$  and  $\mathbf{P}_{iac}$  are prolongation operators (in parameter) from a grid on a type c mesh on  $\Gamma_i^*$  to a grid on a type a mesh on  $\Gamma_i^*$ . Note that  $\mathbf{R}_i$  for  $i = n_{\text{sub}}$ , according to the definition (D.1), is identical to the full diagonal  $64 \times 64$  block of  $\mathbf{R}$  of (19). Note also that  $\mathbf{R}_1$  comes cheaply. The rest of

this appendix is about finding an expression for  $\mathbf{R}_i$  in terms of  $\mathbf{R}_{i-1}$  that is cheap to compute.

Let us split  $\mathbf{K}_{ia}$  into two parts

$$\mathbf{K}_{ia} = \mathbf{K}_{ia}^* + \mathbf{K}_{ia}^\circ, \quad (\text{D.2})$$

where  $\mathbf{K}_{ia}^* = \mathbb{F}\{\mathbf{K}_{(i-1)a}\}$  and  $\mathbf{K}_{ia}^\circ$  is such that

$$\mathbf{K}_{ia}^\circ = \mathbf{P}_{iab} \mathbf{K}_{ib}^\circ \mathbf{P}_{Wiab}^T \quad (\text{D.3})$$

holds to about machine precision, compare (17). The prolongation operators  $\mathbf{P}_{iab}$  and  $\mathbf{P}_{Wiab}$  act from a grid on a type  $\mathbf{b}$  mesh to a grid on a type  $\mathbf{a}$  mesh. It holds that

$$\mathbf{P}_{iac} = \mathbf{P}_{iab} \mathbf{P}_{bc}, \quad (\text{D.4})$$

$$\mathbf{P}_{Wiac} = \mathbf{P}_{Wiab} \mathbf{P}_{Wbc}. \quad (\text{D.5})$$

Summing up, we can rewrite (D.1) as

$$\mathbf{R}_i = \mathbf{P}_{Wbc}^T \mathbf{P}_{Wiab}^T (\mathbf{I}_{ia} + \mathbb{F}\{\lambda \mathbf{K}_{(i-1)a}\} + \lambda \mathbf{P}_{iab} \mathbf{K}_{ib}^\circ \mathbf{P}_{Wiab}^T)^{-1} \mathbf{P}_{iab} \mathbf{P}_{bc}. \quad (\text{D.6})$$

The subsequent steps in the derivation of (22) are to expand the term within parenthesis in (D.6) in a Neumann series, multiply the terms in this series with  $\mathbf{P}_{Wiab}^T$  from the left and with  $\mathbf{P}_{iab}$  from the right, and bring the series back in closed form. The result is

$$\mathbf{R}_i = \mathbf{P}_{Wbc}^T \left[ \left( \mathbf{P}_{Wiab}^T (\mathbf{I}_{ia} + \mathbb{F}\{\lambda \mathbf{K}_{(i-1)a}\})^{-1} \mathbf{P}_{iab} \right)^{-1} + \lambda \mathbf{K}_{ib}^\circ \right]^{-1} \mathbf{P}_{bc}, \quad (\text{D.7})$$

which, in fact, is (22) in disguise. To see this, recall from (D.1) that

$$\mathbf{R}_{(i-1)} \equiv \mathbf{P}_{W(i-1)ac}^T (\mathbf{I}_{(i-1)a} + \lambda \mathbf{K}_{(i-1)a})^{-1} \mathbf{P}_{(i-1)ac}. \quad (\text{D.8})$$

Then

$$\begin{aligned} \mathbb{F}\{\mathbf{R}_{(i-1)}\} &= \mathbb{F}\{\mathbf{P}_{W(i-1)ac}^T (\mathbf{I}_{(i-1)a} + \lambda \mathbf{K}_{(i-1)a})^{-1} \mathbf{P}_{(i-1)ac}\} \\ &= \mathbf{P}_{Wiab}^T (\mathbf{I}_{ia} + \mathbb{F}\{\lambda \mathbf{K}_{(i-1)a}\})^{-1} \mathbf{P}_{iab} - \mathbf{I}_b^\circ, \end{aligned} \quad (\text{D.9})$$

where the second equality uses  $\mathbf{P}_{Wiab}^T \mathbf{P}_{iab} = \mathbf{I}_b$ , see Appendix A. Substitution of (D.9) in (D.7) gives the recursion in the familiar form

$$\mathbf{R}_i = \mathbf{P}_{Wbc}^T (\mathbb{F}\{\mathbf{R}_{i-1}^{-1}\} + \mathbf{I}_b^\circ + \lambda \mathbf{K}_{ib}^\circ)^{-1} \mathbf{P}_{bc}. \quad (\text{D.10})$$



## Appendix E. An inner product preserving scheme

In [4], Bremer describes a scheme that stabilizes the solution to the discretized system (9) on the fine mesh. The scheme can be interpreted as an inner product preserving discretization. In practice it corresponds to making a similarity transformation of the system matrix. While inner product preserving Nyström discretization elegantly solves problems related to stability (the condition number of the system matrix is improved) it does not reduce the number of discretization points (unknowns) needed to achieve a given precision in the solution. Neither does it affect the spectrum of the system matrix (similarity transformations preserve eigenvalues) and hence it does not in any substantial way improve the convergence rate of the GMRES iterative method [48, Lecture 35].

For completeness, we have implemented inner product preserving Nyström discretization in the program `demo1d.m`. The program is a continuation of `demo1b.m` where we also have replaced (3) with the more stable integral equation (25). This should facilitate comparison with the program `demo3b.m` and the results shown in Figure 7.

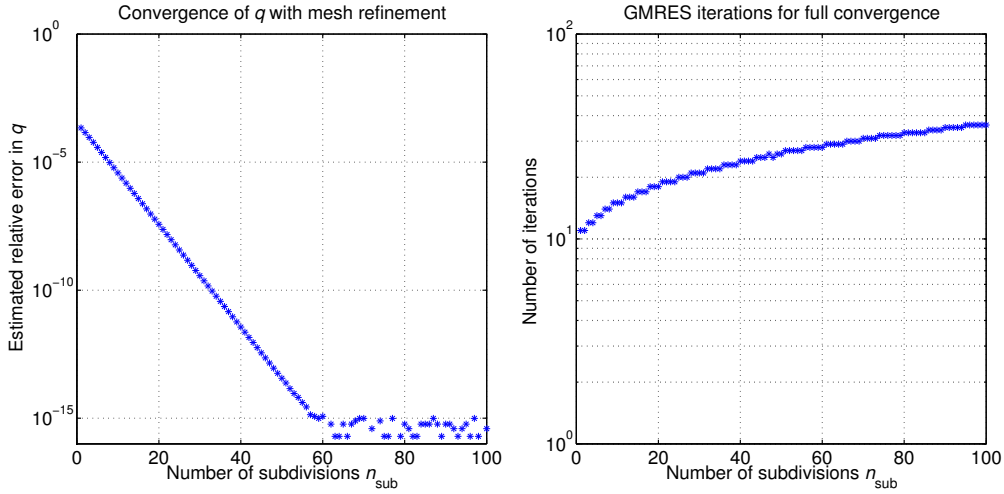


Figure 33: Same as Figure 7, but the program `demo1d.m` is used.

Figure 33 shows results produced by `demo1d.m`. Beyond  $n_{\text{sub}} = 60$  one now achieves essentially full machine precision in  $q$  of (7). Despite this success, inner product preserving Nyström discretization can perhaps not quite compete with the RCIP method in this example. The differences in performance relate to issues of memory and speed. The RCIP method uses a much smaller linear system ( $16n_{\text{pan}}$  unknowns) than does inner product preserving Nyström discretization ( $16(n_{\text{pan}} + 2n_{\text{sub}})$  unknowns). Besides, the RCIP method converges in only eight GMRES iterations, irrespective of  $n_{\text{sub}}$ . See Figure 7.

## References

- [1] E. Akhmetgaliyev and O. P. Bruno, ‘Regularized integral formulation of mixed Dirichlet–Neumann problems’, *J. Integr. Equat. Appl.*, (in press 2017).
- [2] K.E. Atkinson, *The Numerical Solution of Integral Equations of the Second Kind*, Cambridge University Press, Cambridge, 1997.
- [3] J. Bremer, ‘A fast direct solver for the integral equations of scattering theory on planar curves with corners’, *J. Comput. Phys.*, **231**, 1879–1899 (2012).
- [4] J. Bremer, ‘On the Nyström discretization of integral equations on planar curves with corners’, *Appl. Comput. Harmon. Anal.*, **32**, 45–64 (2012).
- [5] J. Bremer, Z. Gimbutas, and V. Rokhlin, A nonlinear optimization procedure for generalized Gaussian quadratures, *SIAM J. Sci. Comput.*, **32** (2010) 1761–1788.
- [6] J. Bremer and V. Rokhlin, ‘Efficient discretization of Laplace boundary integral equations on polygonal domains’, *J. Comput. Phys.*, **229**, 2507–2525 (2010).
- [7] J. Bremer, V. Rokhlin, and I. Sammis, ‘Universal quadratures for boundary integral equations on two-dimensional domains with corners’, *J. Comput. Phys.*, **229**, 8259–8280 (2010).
- [8] O.P. Bruno, J.S. Owall, and C. Turc, ‘A high-order integral algorithm for highly singular PDE solutions in Lipschitz domains’, *Computing*, **84**, 149–181 (2009).
- [9] O.P. Bruno, T. Elling, and C. Turc, ‘Regularized integral equations and fast high-order solvers for sound-hard acoustic scattering problems’, *Int. J. Numer. Meth. Eng.*, **91**, 1045–1072 (2012).
- [10] H. Cheng and L. Greengard, ‘A method of images for the evaluation of electrostatic fields in systems of closely spaced conducting cylinders’, *SIAM J. Appl. Math.*, **58**, 122–141 (1998).
- [11] D. Colton and R. Kress, *Inverse Acoustic and Electromagnetic Scattering Theory*, 2nd ed., Springer, Berlin, 1998.
- [12] J. Englund, ‘A higher order scheme for two-dimensional quasi-static crack growth simulations’, *Comp. Meth. Appl. Mech. Engrg.*, **196**, 2527–2538 (2007).
- [13] A. Girouard and I. Polterovich, ‘Spectral geometry of the Steklov problem’, *J. Spectr. Theory*, **7**, 321–359 (2017).
- [14] L. Greengard and J.-Y. Lee, ‘Stable and accurate integral equation methods for scattering problems with multiple material interfaces in two dimensions’, *J. Comput. Phys.*, **231**, 2389–2395 (2012).
- [15] L. Greengard and V. Rokhlin, ‘A fast algorithm for particle simulations’, *J. Comput. Phys.*, **73**, 325–348 (1987).
- [16] S. Hao, A.H. Barnett, P.G. Martinsson, and P. Young, ‘High-order accurate methods for Nyström discretization of integral equations on smooth curves in the plane’, *Adv. Comput. Math.*, **40**, 245–272 (2014).

- [17] J. Helsing, ‘Fast and accurate calculations of structural parameters for suspensions’, *Proc. R. Soc. Lond.*, **A445**, 127–140 (1994).
- [18] J. Helsing, ‘Thin bridges in isotropic electrostatics’, *J. Comput. Phys.*, **127**, 142–151 (1996).
- [19] J. Helsing, ‘A high-order accurate algorithm for electrostatics of overlapping disks’, *J. Stat. Phys.*, **90**, 1461–1473 (1998).
- [20] J. Helsing, ‘Corner singularities for elliptic problems: special basis functions versus ”brute force”’, *Comm. Numer. Methods Engrg.*, **16**, 37–46 (2000).
- [21] J. Helsing, ‘Integral equation methods for elliptic problems with boundary conditions of mixed type’, *J. Comput. Phys.*, **228**, 8892–8907 (2009).
- [22] J. Helsing, ‘A fast and stable solver for singular integral equations on piecewise smooth curves’, *SIAM J. Sci. Comput.*, **33**, 153–174 (2011).
- [23] J. Helsing, ‘The effective conductivity of random checkerboards’, *J. Comput. Phys.*, **230**, 1171–1181 (2011).
- [24] J. Helsing, ‘The effective conductivity of arrays of squares: large random unit cells and extreme contrast ratios’, *J. Comput. Phys.*, **230**, 7533–7547 (2011).
- [25] J. Helsing and A. Holst, ‘Variants of an explicit kernel-split panel-based Nyström discretization scheme for Helmholtz boundary value problems’, *Adv. Comput. Math.*, **41**, 691–708 (2015).
- [26] J. Helsing and A. Jonsson, ‘On the computation of stress fields on polygonal domains with V-notches’, *Int. J. Numer. Meth. Eng.*, **53**, 433–454 (2002).
- [27] J. Helsing and A. Karlsson, ‘An accurate boundary value problem solver applied to scattering from cylinders with corners’, *IEEE Trans. Antennas Propag.*, **61**, 3693–3700 (2013).
- [28] J. Helsing and A. Karlsson, ‘Determination of normalized electric eigenfields in microwave cavities with sharp edges’, *J. Comput. Phys.*, **304**, 465–486 (2016).
- [29] J. Helsing, R.C. McPhedran, and G.W. Milton, ‘Spectral super-resolution in metamaterial composites’, *New J. Phys.*, **13**, 115005 (2011).
- [30] J. Helsing and R. Ojala, ‘On the evaluation of layer potentials close to their sources’, *J. Comput. Phys.*, **227**, 2899–2921 (2008).
- [31] J. Helsing and R. Ojala, ‘Corner singularities for elliptic problems: Integral equations, graded meshes, quadrature, and compressed inverse preconditioning’, *J. Comput. Phys.*, **227**, 8820–8840 (2008).
- [32] J. Helsing and R. Ojala, ‘Elastostatic computations on aggregates of grains with sharp interfaces, corners, and triple-junctions’, *Int. J. Solids Struct.*, **46**, 4437–4450 (2009).
- [33] J. Helsing and K.-M. Perfekt, ‘On the polarizability and capacitance of the cube’, *Appl. Comput. Harmon. Anal.*, **34**, 445–468 (2013).
- [34] J. Helsing and K.-M. Perfekt, ‘The spectra of harmonic layer potential operators on domains with rotationally symmetric conical points’, *arXiv:1703.01628 [math.AP]*.

- [35] J. Helsing and G. Peters, ‘Integral equation methods and numerical solutions of crack and inclusion problems in planar elastostatics’, *SIAM J. Appl. Math.*, **59**, 965–982 (1999).
- [36] H.V. Henderson and S.R. Searle, ‘On deriving the inverse of a sum of matrices’, *SIAM Rev.* **23**, 53–60 (1981).
- [37] N.J. Higham, *Accuracy and stability of numerical algorithms*, SIAM, Philadelphia, 1996, 92–97.
- [38] W. Kahan, ‘Further remarks on reducing truncation errors’, *Comm. ACM*, **8**, 40 (1965).
- [39] A. Klöckner, A. Barnett, L. Greengard, and M. O’Neil, ‘Quadrature by expansion: A new method for the evaluation of layer potentials’, *J. Comput. Phys.*, **252**, 332–349 (2013).
- [40] W.Y. Kong, J. Bremer, and V. Rokhlin, ‘An adaptive fast direct solver for boundary integral equations in two dimensions’, *Appl. Comput. Harmon. Anal.*, **31**, 346–369 (2011).
- [41] R. Kress, ‘On the numerical solution of a hypersingular integral equation in scattering theory’, *J. Comput. Appl. Math.*, **61**, 345–360 (1995).
- [42] D. McA. McKirdy, H.A. Shute, D.T. Wilton, ‘Estimation of Fichera-type eigenvalues in the vicinity of sharp corners in dielectric media using standard functions’, (preprint 2017).
- [43] R.C. McPhedran, L. Poladian, G.W. Milton, ‘Asymptotic studies of closely spaced, highly conducting cylinders’, *Proc. R. Soc. Lond. A* **415**, 185–196 (1988).
- [44] M. Mitrea, ‘Boundary value problems and Hardy spaces associated to the Helmholtz equation in Lipschitz domains’, *J. Math. Anal. Appl.*, **202**, 819–842 (1996).
- [45] R. Ojala, ‘A robust and accurate solver of Laplace’s equation with general boundary conditions on general domains in the plane’, *J. Comp. Math.*, **30**, 433–448 (2012).
- [46] Y. Saad and M.H. Schultz, ‘GMRES: A generalized minimal residual algorithm for solving nonsymmetric linear systems’, *SIAM J. Sci. Stat. Comp.*, **7**, 856–869 (1986).
- [47] K. Serkh and V. Rokhlin, ‘On the solution of elliptic partial differential equations on regions with corners’, *J. Comput. Phys.*, **305**, 150 – 171 (2016).
- [48] L.N. Trefethen and D. Bau, III, *Numerical Linear Algebra*, SIAM, Philadelphia, PA, 1997.
- [49] <https://www.unibw.de/bauv1/forschung/cocos/singexp.html>